AD-A098 586 NAVAL RESEARCH LAB WASHINGTON DC F/G 14/5
REPORT OF NRL PROGRESS.(U)
NOV 79

UNCLASSIFIED NL

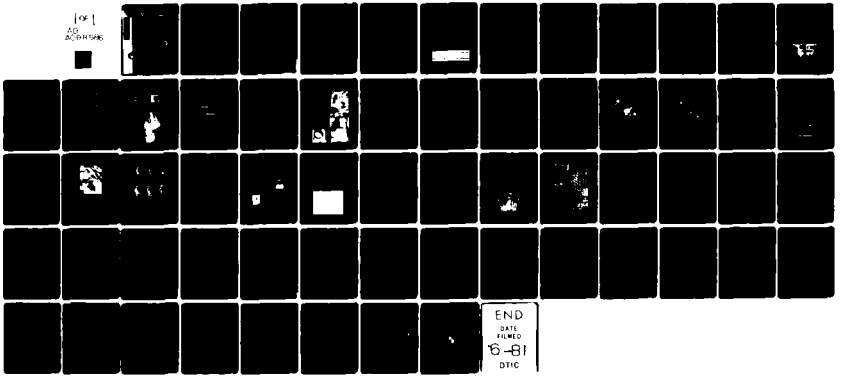

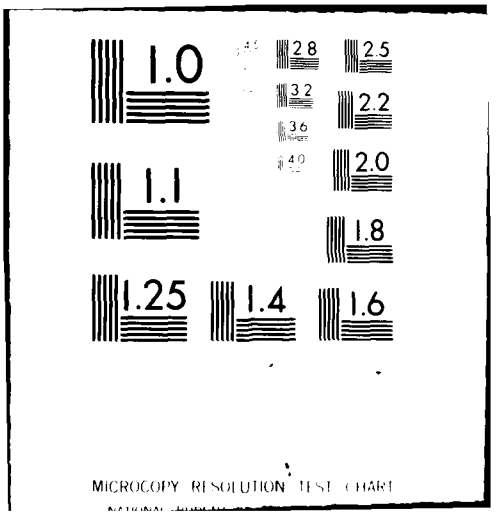
1.0
2.8
2.5
3.2
2.2
3.6
2.0
4.0
1.1
1.8
1.25
1.4
1.6
MICROCOPY RESOLUTION TEST CHART

(6)

REPORT OF NRL PROGRESS

NAVAL RESEARCH LABORATORY
Washington, D. C.

Over Fifty Years of Science for the Navy and the Nation

PUBLICATION TO BE DISCONTINUED

Publication of the *Report of NRL Progress* will be discontinued with the December 1979 issue, thus ending thirty-four years of creditable research reporting. This decision was made after careful consideration of the results of a recent survey and a recent zero-baseline study of the report. As a result of these studies, it was decided that it was not cost-effective to continue publishing the *Report of NRL Progress* when there were other means available to disseminate the same information.

CONTENTS

November 1979

Development and Application of Electrographic Image Detectors

George R. Carruthers and Harry M. Heckathorn

E. O. Hulburt Center for Space Research

Electrography is, in principle, both the simplest and one of the most photometrically accurate methods of electronic imaging. This paper discusses the basic principles of electrography, its advantages over conventional photography and other methods of electronic imaging, its practical difficulties, and the methods and special requirements for reduction and analysis of electrographic images. Electrographic detectors, primarily sensitive in the vacuum-ultraviolet wavelength range, have been under development in NRL's Space Science Division since 1965 for use in ultraviolet astronomy and ultraviolet measurements of the terrestrial upper atmosphere. These investigations have primarily involved flight of these detectors in sounding rockets, but these devices were also used in the *Apollo 16* and *Skylab 4* missions. Devices presently operational or under development are planned or proposed for space-science investigations in space-shuttle missions. We currently are using a visible-sensitive Kron electrographic detector for ground-based astronomical observations, and are developing middle-ultraviolet and visible-light-sensitive versions of our own detectors. Electrographic detectors also have applications in other fields of scientific research. One such application is in observations of the earth from space.

INTRODUCTION

This paper is concerned with a particular area of electronic imaging technology known as *electrography*, literally, writing with electrons, analogous to photography, writing with photons. We will discuss the basic principles, advantages, and practical difficulties of the electrographic method in comparison with other, more common, methods of electronic imaging. We will then discuss specifically the developments of electrographic detectors carried out in the NRL Space Science Division over the past 15 years; space does not permit more than brief mention of developments elsewhere, but these may be found in the references provided.

An important aspect of the practical application of electrographic devices is the extraction of useful data from the recorded images. Although the methods are similar to those used to analyze photographic images, the significant potential advantages of electrography over photography in photometric accuracy and dynamic range require special attention to the analysis techniques.

The application of the NRL-developed devices to space astronomy and ultraviolet measurements of the terrestrial upper atmosphere are discussed, both in past space missions and in proposed future missions. Finally, we discuss current and potential applications of these devices to laboratory measurements and applications in areas outside of our own fields of space-science research.

THE ELECTROGRAPHIC PROCESS

Electrography is, at the same time, both the simplest in principle and one of the most photometrically accurate methods of electronic imaging. An electrographic detector consists of three main components: a photocathode which emits electrons when it is illuminated with electromagnetic radiation in the wavelength range to which it is sensitive; a means for accelerating and focusing the photoelectrons, so as to produce an "electron image" which is a duplicate of the optical, or photon, image projected on the photocathode; and a recording emulsion which is quite similar to an ordinary photographic emulsion, but in

which blackened grains (after processing) are the result of electron impacts rather than exposure to photons. The space between the photocathode and the recording emulsion must be maintained at high vacuum, as in most other electronic vacuum tubes, to avoid effects of collisions between the photoelectrons and residual gas molecules; as will be discussed later, other restrictions may be imposed by the chemical reactivity of the photocathode material.

The electrographic process can provide much higher sensitivity and photometric accuracy than conventional photography. The improved sensitivity is the result of the fact that the photoemissive quantum efficiency (photoelectrons per incident photon) of photocathode materials can be much higher than the effective quantum efficiency of a photographic emulsion (blackened grains per incident photon).

Photocathode quantum efficiencies can be as high as 20 to 30% in the visible range and in excess of 50 to 60% in the far-ultraviolet and x-ray ranges, whereas the quantum efficiencies of even the fastest photographic emulsions in recording photons directly are only of the order of 1 to 3%. Each photoelectron released from a photocathode, if accelerated to sufficiently high energy, of the order of 15 to 30 keV, will blacken one or more grains on impact with a suitable recording emulsion (nuclear-track emulsions, such as those used for detecting cosmic rays, are most generally used) with very high probability; typically, a track of several blackened grains is produced. Therefore, the effective sensitivity gain of electrography over photography is nearly the ratio of the photocathode quantum efficiency to the photographic-emulsion quantum efficiency.

Conventional photography, in addition to having a low maximum quantum efficiency, has the additional difficulty, particularly where photometric accuracy is important, that the effective quantum efficiency depends on, among other things, source intensity and duration of exposure. This is in part due to the fact that many more than one photon are required to render a grain developable. This results in a certain inertia or threshold which must be overcome before the formation of a latent image is possible—a fact which tends to limit the performance of the photographic emulsion when the number of photons per unit area is low. Also, for a given photographic grain, if the time interval between exposure to photons is too long or too short the cumulative benefits of increased exposure time are not fully realized, resulting in reciprocity failure.

In the electrographic process, on the other hand, there is complete reciprocity between image blackening and the algebraic product of exposure time and source intensity. Also, there is no threshold effect at low light levels. Therefore, at low light levels, such as are typical in astronomical observations and in many laboratory investigations, the effective sensitivity gain of electrography over photography can be significantly greater than the ratio of quantum efficiencies measured under conditions optimum for the photographic emulsion.

The greatly improved photometric accuracy of the electrographic process in comparison to conventional photography is also due to the much-finer grain and lower background of the emulsions used in electrography vs "fast" photographic emulsions. This results in a much wider dynamic range in electrographic recording; i.e., a much wider range of integrated intensities can be usefully recorded in a single exposure. Over a large portion of this range, the optical density of the processed emulsion, as given by a microdensitometer, is directly proportional to the integrated photoelectron flux and, hence, the light flux incident on the photocathode ($d = \log_{10} I_0/I$, where I_0 is the incident light intensity and I is the transmitted light intensity). In other words, the electrographic process is *linear*, or nearly so, over a wide integrated intensity range.

An additional benefit of the use of fine-grained recording emulsions is that electrography is potentially capable of significantly better resolution than conventional photography, particularly with fast emulsions. When combined with the wide dynamic range of electrography, this attribute results in a much larger information-storage capacity on a given area of emulsion. This attribute, together with linearity of response, relative sensitivity, and other pertinent properties of electron-sensitive emulsions for use in astronomical electrography have been described by Cohen and Kahan (1) and by Griboval et al. (2).

Since the spectral response of an electrographic detector is determined by the photocathode rather than by the recording emulsion, and since photocathodes can be selected which are sensitive only below

characteristic threshold wavelengths, it is possible to tailor the long-wavelength limit of sensitivity of an electrographic detector without the use of auxiliary filters. For example, it is possible to make detectors sensitive in the middle or far ultraviolet but totally insensitive to longer-wavelength visible light. This is not possible with current photographic emulsions.

It is also useful to compare electrography with other methods of electronic imaging. For example, a commonly used electronic imaging device is an *image intensifier.* In such a device, a *phosphor screen* is placed at the electron image plane, instead of the recording emulsion used in an electrographic device; the portions of the devices forward of the electron image may be identical. When a highly energetic photoelectron strikes the phosphor screen, several hundred visible-light photons may be produced. A portion of these can be coupled to photographic film by means of a lens or by fiber optics. By coupling two or more image intensifiers, photon gains of up to 10^4 or 10^5 may be realized, allowing the blackening of, on the average, one or more grains in the photographic emulsion for each primary photoelectron. Hence, the quantum efficiency gain of the image intensifier is about the same as that of an electrographic detector with the same photocathode. Like the latter, it can be made sensitive in the UV but insensitive in the visible. An image intensifier is also known as an *image converter* when the wavelength range to which the photocathode is sensitive is different from that of the light output of the phosphor.

However, image-intensified photography still suffers most of the photometric disadvantages of conventional photography (see Fig. 1). In addition, there is some loss of image resolution due to the phosphor screen, the transfer lens or fiber optics, and light scattering in the photographic film; this resolution loss is greater if more than one image-intensifier stage is used. Therefore, the net resolution achieved is less than that of conventional photography and considerably less than is achievable with the electrographic method.

In comparison with electronic imaging devices which produce an electrical signal readout ("television type" detectors), the electrographic device has both potentially better resolution and the capability of recording a larger image area. The product of image area and inverse resolution is the total number of resolvable picture elements, or *pixels*, in the image. Thus, electrographic detectors can record a much larger number of pixels per frame than can present TV-type detectors. Even the highest-resolution television detectors currently available can record only of the order of $1000 \times 1000 = 10^6$ pixels per frame. A large-format, high-resolution electrographic camera presently operational at NRL in the far UV, on the other hand, can record an image more than 100-mm square with a resolution of better than 10 μm, i.e., $10{,}000 \times 10{,}000 = 10^8$ pixels. There is no fundamental reason why much larger images (200 X 200 mm or larger) could not be handled.

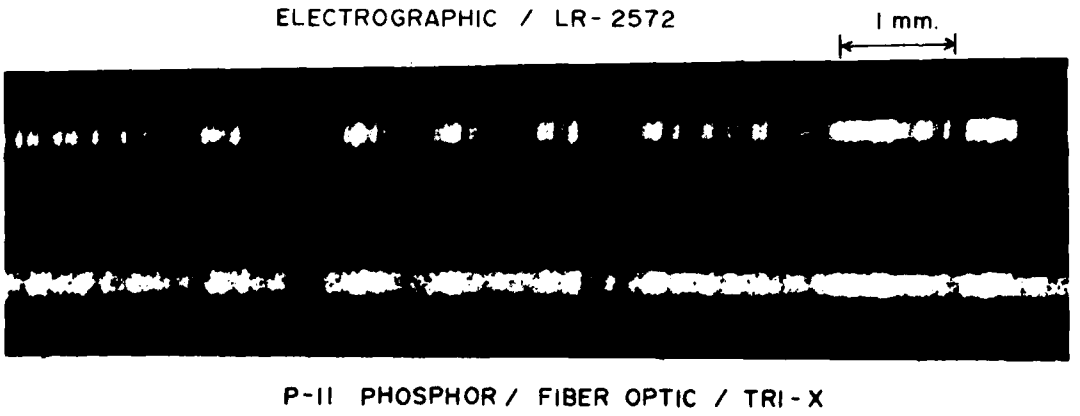

Fig. 1 – Comparison of spectra of a laboratory light source, taken with the same Schmidt electronic image device, with identical exposure times and operating voltages, but using two different methods of readout: (top) electrographic recording; (bottom) photographic recording on Tri-X film from a phosphor screen/fiber optic output.

In summary, for applications where speed and photometric accuracy are not of primary concern, photographic emulsions have some attractive features and are still widely used. They are readily available and inexpensive; there is no fundamental limitation on image area; they require no power; and they are lightweight. TV-type detectors are most useful when the image must be studied in real time or for remote operations where emulsion retrieval is not feasible. Electrography, on the other hand, is most useful when the number of photons per unit area on the detector is small, when photometric performance is important, and when the required resolution (coupled with a large number of pixels) is high.

With all its potential advantages, one may ask why electrography is not more widely used, particularly in comparison to image intensifiers and television detectors, in ground-based astronomy and laboratory measurements. Largely, this is due to the fact that, although the electrographic detector is very simple in principle, its use is greatly complicated in practice by the fact that photocathodes sensitive in the visible, infrared, and near-to-middle ultraviolet are very reactive chemically. As a result, they suffer very rapid and irreversible loss of photoelectric sensitivity if exposed to gases such as oxygen and water vapor, even at pressure levels of less than 0.1 mPa (10^{-6} torr) (3). The emulsions used in electrography, like those used in photography, are gelatin based and contain significant amounts of water and other volatiles which outgas in vacuum. Thus, even in a high-vacuum environment, the photocathode is rapidly degraded by the outgassing of the recording emulsion. The practical application of electrography longward of 2000 Å requires development of means for protecting the photocathode from this outgassing. On the other hand, photocathodes sensitive only in the vacuum ultraviolet (below 2000 Å) are far less chemically reactive and it is much easier to construct and use these electrographic detectors than those with photocathodes sensitive at longer wavelengths.

In the following paragraphs, we discuss in more detail the major components of electrographic detectors: photocathodes, electron-optical focusing methods, and means for protecting the photocathodes from outgassing of the recording emulsions.

Photocathodes

Two basic types of photocathodes may be distinguished, regardless of the specific photosensitive material (see Fig. 2): semitransparent photocathodes; and opaque, or front-surface, photocathodes.

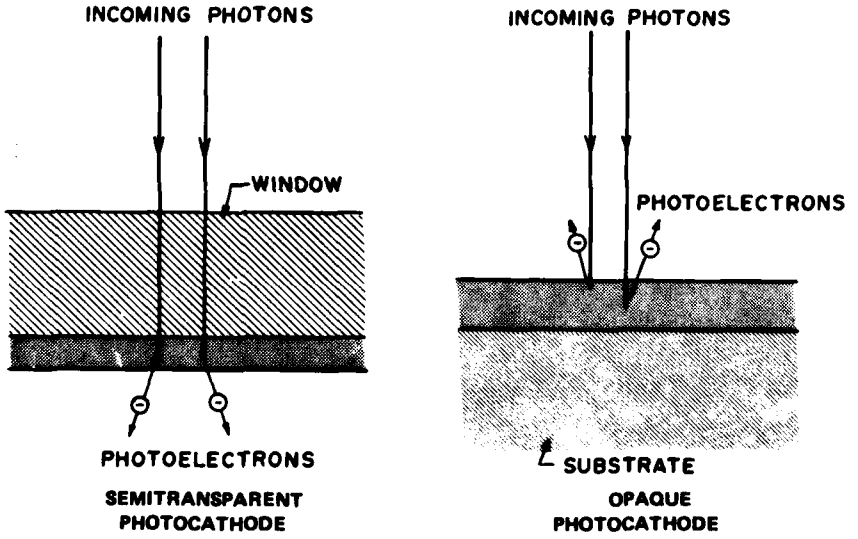

Fig. 2 – Operating principles of semitransparent and opaque photocathodes.

The semitransparent photocathode is the type most commonly used in photomultipliers, image intensifiers, and electrographic detectors. In this type, the photoemissive substance is deposited on the inside surface of a window which forms the face of the detector through which the light enters. In some cases the window material may be selected to serve not only as a support for the photocathode but also as a filter to absorb incoming radiation with wavelengths shortward of a particular limit characteristic of the substrate. Light passing through the transparent window causes photoelectrons to be emitted which travel in the *same* direction as the incident photons. The photoemissive layer must be thick enough to absorb a large portion of the incoming light, but not so thick that photoelectrons produced near the photocathode-window interface cannot escape into the vacuum inside the device. In practice, these are conflicting requirements; one must settle on a best compromise thickness to maximize the photocathode quantum efficiency.

The opaque photocathode, on the other hand, does not require a window; it can be supported on a metallic substrate. Since the emitted photoelectrons travel in the direction *opposite* to that of the incident light, the photocathode layer can be as thick as needed to absorb all the incident radiation; the escape of photoelectrons produced near the light-incident surface is not thereby reduced. Therefore, particularly in

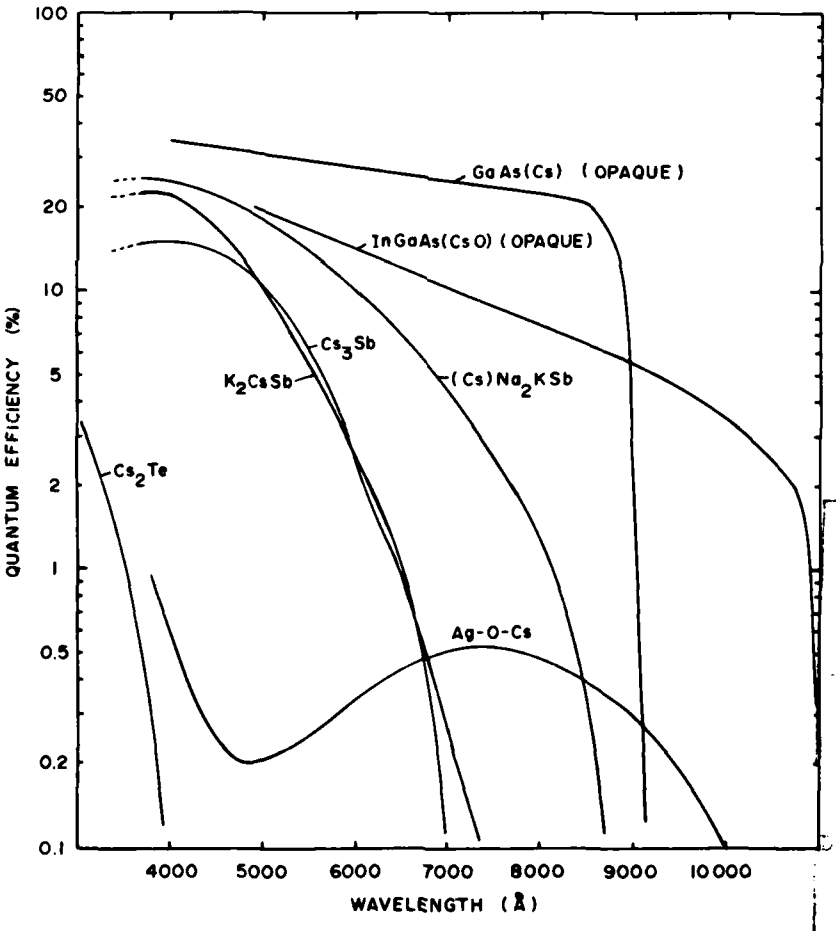

Fig. 3 -- Typical spectral response curves of photocathodes useful in the visible, near-infrared, and near-ultraviolet spectral ranges. All are semitransparent photocathodes except as noted. The short wavelength ends of the response curves are determined by the transmission characteristics of the window materials used.

the ultraviolet, opaque photocathodes can have considerably higher quantum efficiencies than semitransparent photocathodes of the same material. Since the absorption losses of a window can be eliminated, it is possible for the device to be sensitive in the extreme ultraviolet wavelength range below 1050 Å, where all conventional window materials become opaque. The main drawback of the opaque photocathode, however, is the difficulty of simultaneously accommodating a photon-optical system to project an optical image onto the photocathode and an electron-optical system for accelerating, focusing, and recording the emitted photoelectrons.

Figures 3 and 4 show typical spectral-response curves for opaque and semitransparent photocathodes useful in the wavelength range 1000 to 10,000 Å. In general, the longer the wavelength of the photosensitivity threshold, the more reactive the photocathode and the more difficult it is to preserve from degradation by contaminant gases. The commonly used photocathodes are based on compounds of alkali metals, such as cesium, with semimetals such as antimony (for the near-visible spectral range) or tellurium (for the middle ultraviolet). Alkali halides, such as cesium iodide, are useful in the far ultraviolet. Photocathodes based on the so-called III-V compounds such as gallium arsenide, activated by exposure to cesium, have been recently developed for the near infrared.

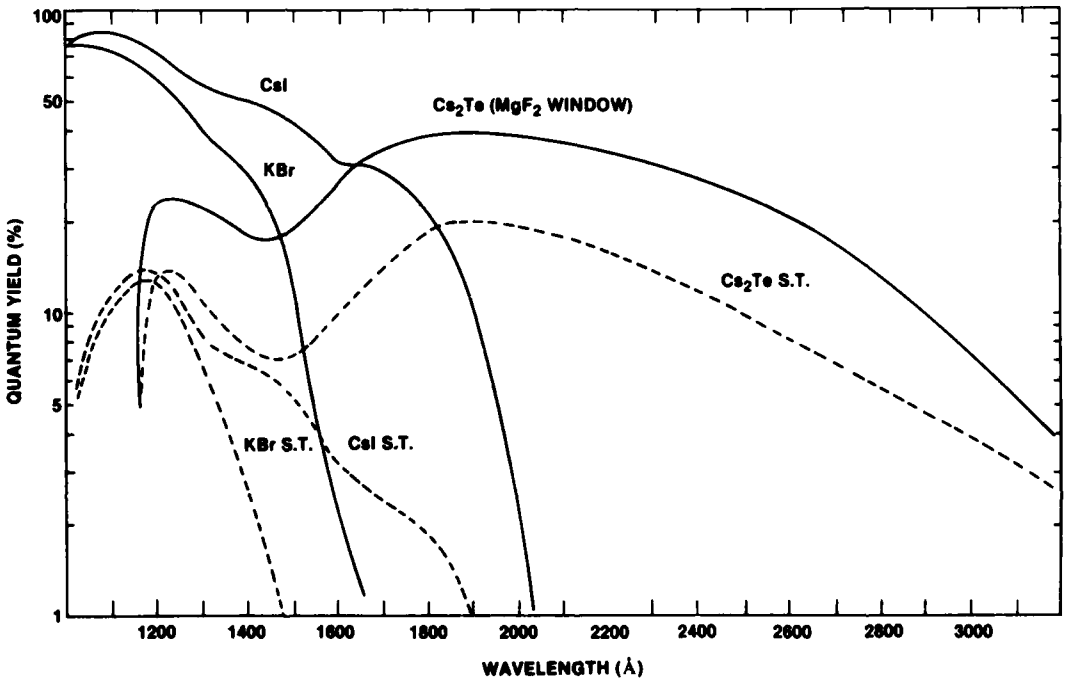

Fig. 4 – Typical spectral response curves of semitransparent and opaque photocathodes for the middle- and far-ultraviolet spectral ranges.

Electron Optical Focusing Methods

Two primary methods of electron-optical image formation, electrostatic focusing and magnetic focusing, have been used in electrographic detectors; these methods are also used in many other types of electronic imaging devices, such as image intensifiers. They are illustrated in Fig. 5 for devices with semitransparent photocathodes.

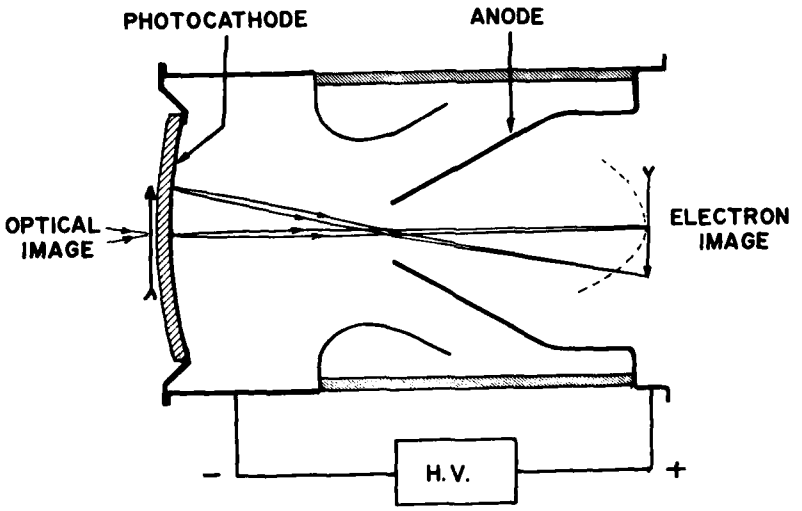

(a)

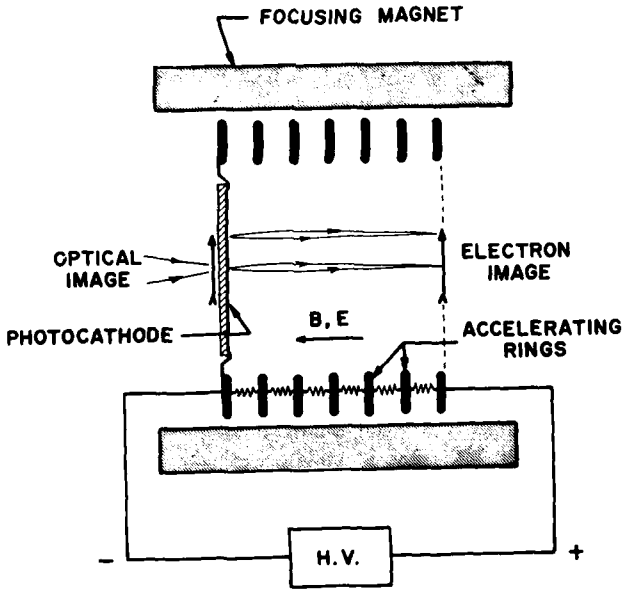

(b)

Fig. 5 – Two methods for accelerating and focusing photoelectrons to produce an electron image: (a) electrostatic focusing; (b) magnetic focusing. In an electrographic device, an electron-sensitive emulsion is placed in the electron image plane.

In electrostatic focusing, one or more properly shaped electrodes are maintained at a positive potential relative to the photocathode, producing an electric field of such a configuration as to act as an electron lens. Electrons passing through this field region are focused in a manner very similar to that of a convex lens focusing light rays. As in the case of a convex lens, the electron image is inverted relative to the image on the photocathode. Best focus conditions are realized when both the photocathode and the electron image are curved and are concave toward each other; however, the depth of electronic focus is sufficiently great that the electron image can often be recorded on a flat surface with little loss in resolution. However, best electron-image quality is obtained on the optical axis, and the image resolution degrades outward from this axis. The requirement for a curved photocathode is a drawback, particularly in the ultraviolet, because of the difficulty of coupling a flat photon image to a curved surface.

In magnetic focusing, the photocathode and electron image are flat and parallel to each other. The photoelectrons are accelerated by maintaining the image plane at positive potential relative to the photocathode; however, the focusing is accomplished by a magnetic field, coaxial with the electric field, which is produced by a surrounding solenoid or cylindrical magnet. The focus condition corresponds to the time that a photoelectron takes to orbit a magnetic field line in the plane perpendicular to the optical axis; this time is exactly equal to the time the photoelectron takes to travel from the photocathode to the electron image plane, or it is an integral submultiple thereof. Magnetic focusing has potentially better resolution than electrostatic focusing, and more importantly, this resolution is uniform over the entire image area. Realization of this goal requires highly uniform electric and magnetic fields. The drawback of the magnetic-focusing method is the requirement for the external magnet or solenoid, which adds to the size and weight of the device.

Methods for Photocathode Protection

Two basic methods have been developed for protecting photocathodes from emulsion outgassing, cooling of the recording emulsion to a very low temperature to inhibit its outgassing, and use of a thin barrier membrane between the photocathode and the emulsion (usually in contact with the latter) which is gastight but is transparent to highly energetic electrons.

The first method was developed by A. Lallemand in France; Lallemand was, in fact, the first to suggest the electrographic technique (4) and the first to develop a working device (5,6). In the Lallemand detector, the photocathode is prepared and kept in a separate, sealed container within the device while the recording plates are installed, the device evacuated, and the plates cooled to liquid nitrogen temperature. (The vapor pressure of the H_2O is less than 1 pPa (10^{-14} torr) at 100 K.) The photocathode is then removed from its container and placed in the proper position within the device, and the observations are made. At the conclusion of the observations, air is let into the device, destroying the photocathode in the process of retrieving the exposed plates; hence, a new photocathode as well as a new set of plates is required for each series of observations.

A variation of this method, developed by G. Kron and co-workers (7), uses a vacuum-tight gate valve between the photocathode and recording plate (see Fig. 6). When this valve is closed, plates can be installed or removed from the device without air reaching the photocathode. Therefore, a single photocathode can be used for many series of observations over periods of months or years without marked deterioration. We currently use a Kron detector at McDonald Observatory for ground-based astronomical observations.

The second approach to photocathode protection is dependent on the selection or development of a suitable material for the barrier membrane (or Lenard window). Such a material must be available in sheets thin enough to transmit electrons of 30- to 40-keV energy with reasonably high efficiency, yet must be impervious to gas molecules and must be strong enough to withstand pressure differentials (depending on the particular device) of up to one atmosphere. The material must be capable of withstanding vacuum bakeouts at temperatures up to 300 to 400°C; such bakeouts are a necessary step in the processing of devices utilizing reactive photocathodes, to eliminate all sources of outgassing within the device prior to preparation or introduction of the photocathode.

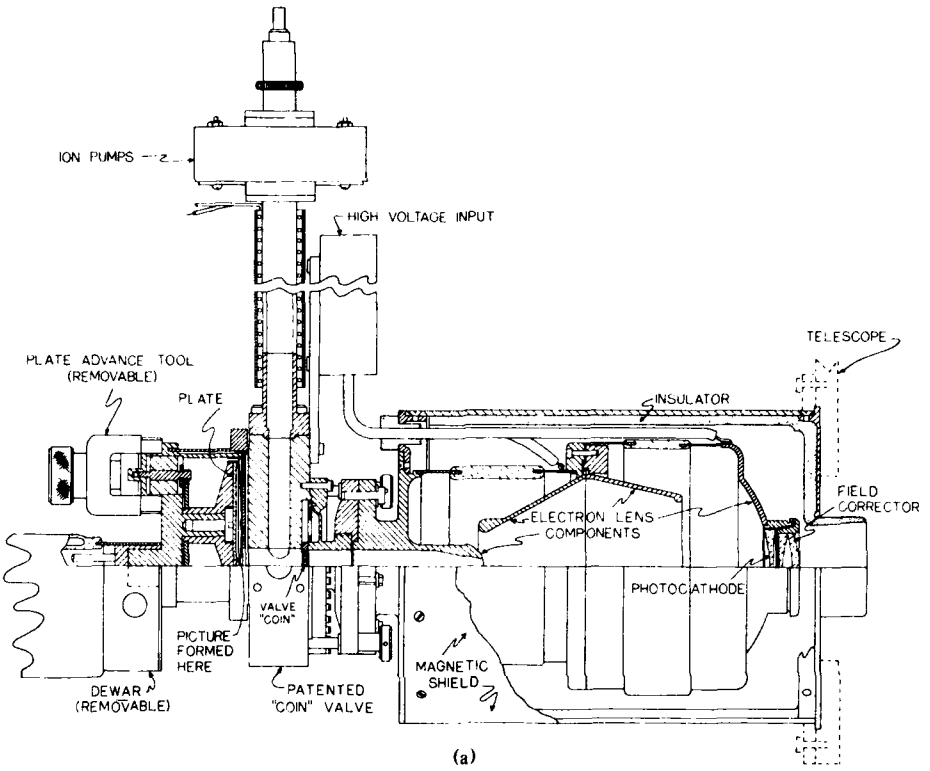

(a)

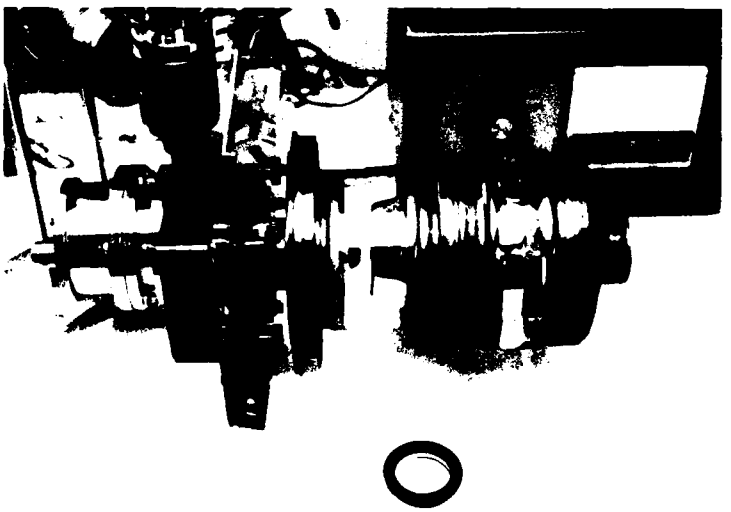

(b)

Fig. 6 – Kron electrographic camera. In this device, developed for use in ground-based astronomy in near-visual wavelengths, the photocathode is protected from emulsion outgassing by cooling the emulsion to liquid nitrogen temperature during exposures; the "coin valve" is closed to protect the photocathode from exposure to air during plate changes: (a) diagram; (b) photograph.

In devices developed by McGee and co-workers at the Imperial College in London (8), thin mica is used as the membrane; it is of a size and thickness such that it can withstand full atmospheric pressure differential. This greatly simplifies the device and its application, since the recording film is simply pressed against the output window to record the photoelectrons. However, the Spectracon, as it is called, is limited to rather small image formats as a result. In a variation developed by McMullan of the Royal Greenwich Observatory (9), the mica window is not required to withstand full atmospheric pressure, an airlock being used to bring the emulsion into contact with the window for exposures, and so it can be much larger than in the case of the Spectracon. Detectors with image sizes up to 80 mm in diameter are now in routine operation. A device developed by P. Griboval at the University of Texas (10) is similar to the McMullan detector, except that the barrier membrane is made of a polyimide plastic; this material is much easier to obtain and use than is thin mica, but it can withstand vacuum bakeouts at temperatures above 200°C. The currently operational Griboval detector has a 50-mm image diameter, but versions with much larger image sizes are under development both at the University of Texas and at NRL.

Because of the complexities involved in the use of practical electrographic detectors (liquid nitrogen cooling, vacuum airlocks, etc.) compared to the use of image intensifiers with photographic recording, electrography has not had as widespread application in astronomy and other fields of research as has the latter technique. However, a combination of improved reliability and ease of operation in newer versions of electrographic detectors and more widespread realization within the scientific community of the unique photometric and other advantages of the electrographic technique will likely increase its arena of application in the near future.

FAR ULTRAVIOLET ELECTROGRAPHIC DETECTORS

As was mentioned previously, it is much easier to construct and use electrographic detectors sensitive in the far-ultraviolet (below 2000 Å) spectral range than at longer wavelengths. This is because materials such as the alkali halides can be used for photocathodes; these can be exposed to dry air at atmospheric pressure without adverse effect, and they are not harmed by emulsion outgassing at reasonable vacuum conditions, less than 10 mPa (10^{-4} torr). Therefore, it is not necessary to cool the emulsions, barrier membranes, etc. for photocathode protection. In the NRL Space Science Division over the past 15 years, we have developed a series of such electrographic detectors for use in our programs of far-ultraviolet astronomy and far-ultraviolet measurements of the upper atmosphere (11-14). These applications to our research programs, and possible other applications of these detectors, are discussed in later sections.

As can be seen from Fig. 4, in the far-ultraviolet spectral range the advantages of opaque photocathodes over semitransparent photocathodes are particularly marked. Therefore, we have combined the use of Schmidt and all-reflecting optical systems with the use of opaque alkali halide photocathodes in a series of instruments intended for wide-field ultraviolet imagery and spectrography (see Figs. 7 and 8). Photographs of some of the instruments used in our rocket programs are shown in Fig. 9. Table 1 lists the apertures and focal ratios of instruments we have used in various flight missions (see page 13).

The two most recent versions of our electrographic Schmidt cameras are a microchannel-intensified version of the 75-mm aperture, f/1 unit and a 150-mm aperture, f/2 camera, the largest of this type of detector we have developed. Figure 10 is a diagram of the microchannel-intensified camera, and Fig. 11 is a diagram of the large Schmidt camera, with a new type of permanent-magnet focusing assembly currently under test and planned for future flights of this camera.

The microchannel-intensified camera (15) is intended for applications involving the detection and measurement of extremely faint, diffuse sources. The microchannel plate multiplies each photoelectron by a factor of about 100; the output electron "bunches" are then reimaged onto the final recording film. Unlike in "conventional" electrography, the "signature" of each electron bunch on the final processed emulsion is readily measurable with microdensitometer apertures comparable to the resolution of the

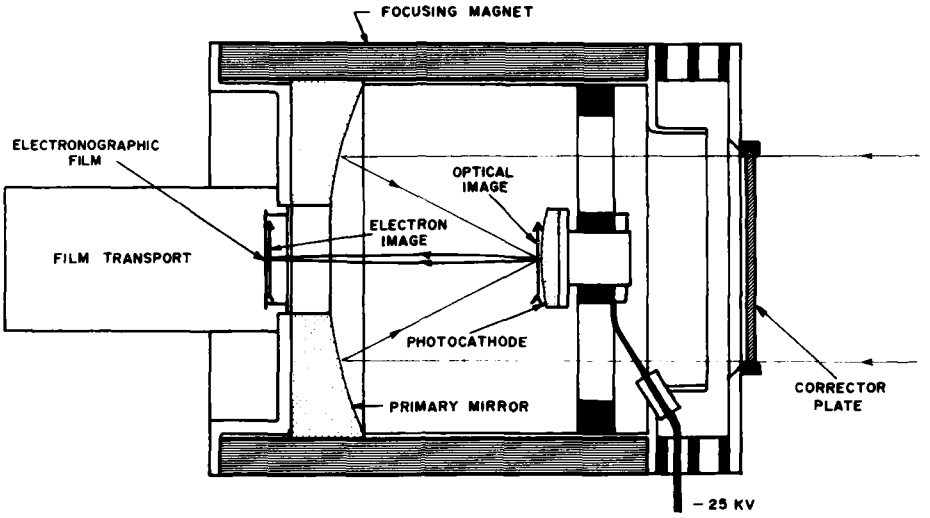

Fig. 7 – Operating principle of the electrographic Schmidt cameras, developed at NRL, which use opaque alkali halide photocathodes for sensitivity in the far ultraviolet.

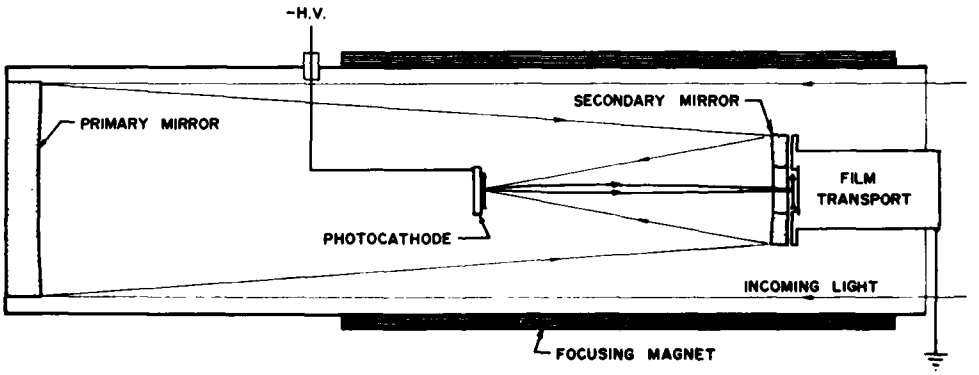

Fig. 8 – Electrographic camera using a two-mirror, all-reflective optical system and opaque photocathode. This device has been used mainly with an objective grating for stellar ultraviolet spectrography.

electrographic camera; in essence we are able to "count" single photoelectrons emitted by the photocathode. This provides improved sensitivity for detection of weak sources, although at the expense of dynamic range and statistical accuracy in the measurement of stronger sources.

We have also been developing electrographic detectors having semitransparent alkali halide photocathodes. These, unlike the devices discussed above, are intended for use with separate, external optical systems. As mentioned previously, although the quantum efficiency of a semitransparent photocathode is not as high as that of an opaque photocathode, the former is generally much easier to integrate into most detector/optical-system combinations. For example, in astronomical applications a semitransparent photocathode detector is easier to use at the focus of a large telescope. There are also practical limits to the size of systems with integrated optics and opaque photocathode, such as those discussed previously; these are in part set by the fact that the inside diameter of the focusing magnet assembly must be larger than the diameter of the light-collecting aperture.

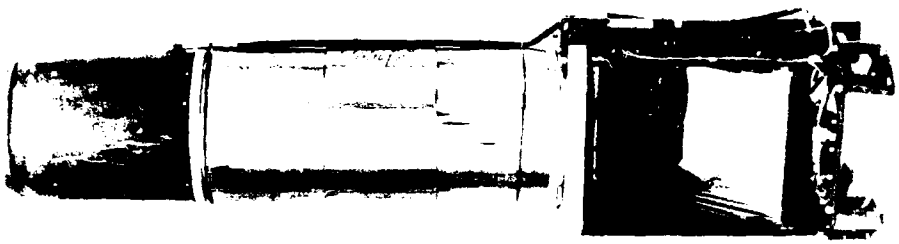

(b)

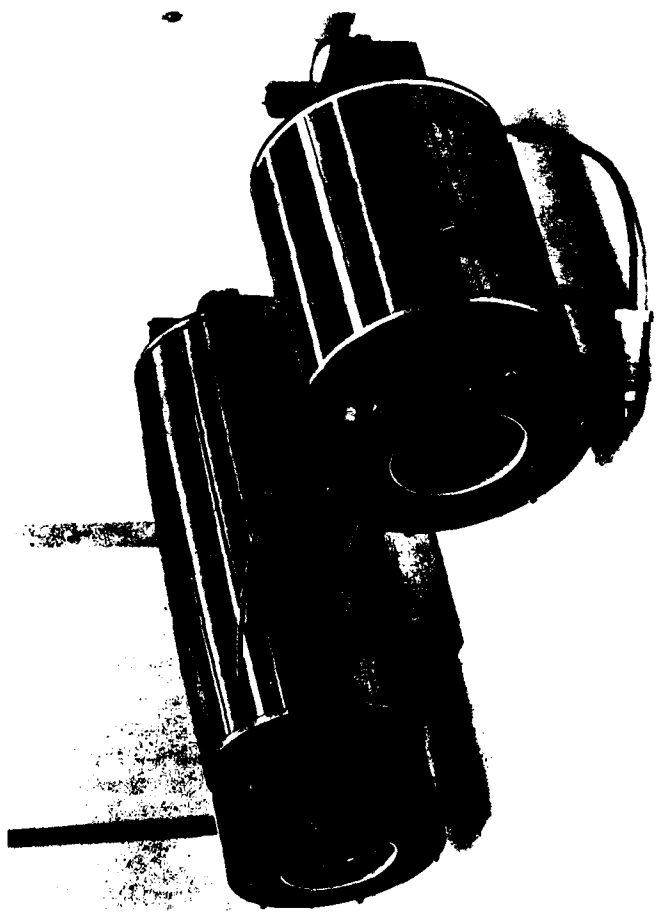

(a)

Fig. 9 – Electrographic cameras used in the NRL far ultraviolet astronomy program: (a) two electrographic Schmidt cameras, 75-mm apertures with f/1 and f/2 focal ratios; (b) all-reflecting spectrograph based on 150-mm aperture, f/3.2 optical system.

Table 1 – NRL Far-Ultraviolet Electrographic Schmidt and All-Reflecting Cameras

Camera Types	Aperture (mm)	Focal Ratio	Year (1st Flight)
Schmidt	50	1.0	1966
	100	1.5	1967
	75	1.0	1970
	75	2.0	1974
	150	2.0	1976
All-Reflecting	150	1.6*	1967
	150	3.2*	1971
	75	2.0†	1974

*Schwarzschild optical system
†Bowen optical system (secondary mirror 365-mm diameter)

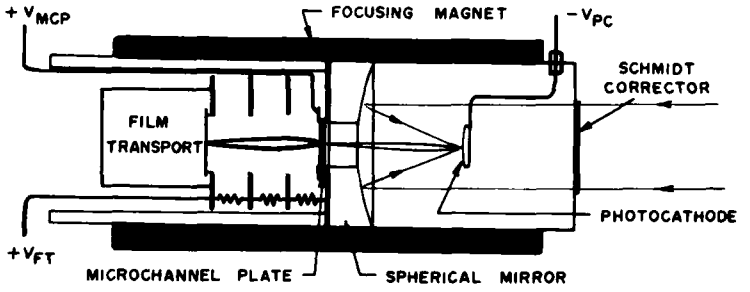

Fig. 10 – Electrographic Schmidt camera incorporating a microchannel plate for electron image intensification.

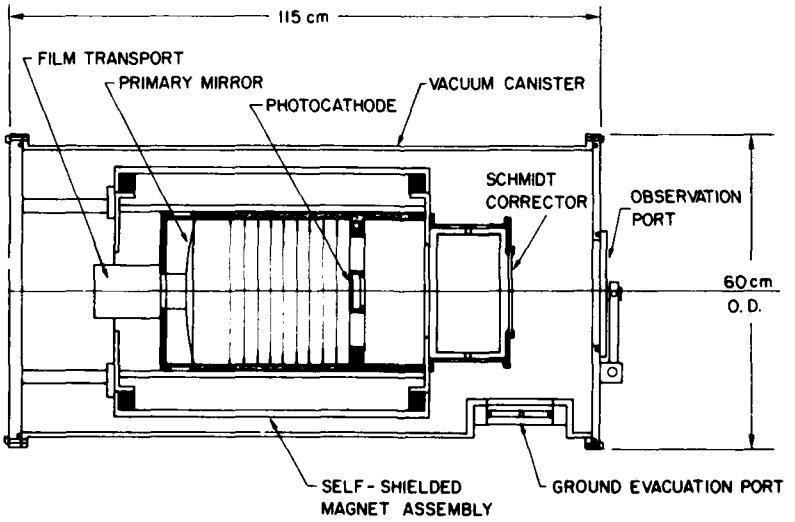

Fig. 11 – The 150-mm aperture, f/2 electrographic Schmidt camera, with new high-uniformity, self-shielded permanent magnet focusing assembly. The instrument is shown in a configuration adaptable either to sounding rocket or space-shuttle missions.

The NRL development of semitransparent photocathode electrographic detectors has been largely supported by NASA, and has been concerned with demonstrating the feasibility of large-format, high-resolution detectors for potential use with astronomical telescopes to be flown in space-shuttle/Spacelab missions (16). A detector having a 123-mm-diameter image format, sensitive in the 1230- to 2000-Å range (CsI photocathode on CaF_2 window), was constructed and tested, using alternately a cylindrical permanent magnet and a superconducting solenoid to provide the focusing magnetic field (see Fig. 12).

With both magnetic-focusing systems, the best resolution obtained in laboratory tests was well in excess of 120 line pairs per millimeter (lp/mm); however, with the cylindrical permanent magnet the resolution over the 123-mm diameter was not uniform because of variations of the magnetic field strength over this diameter. The superconducting solenoid provided a much more uniform field and hence much more uniform resolution. The primary reason for using the superconducting solenoid, however, was to perform tests at very high magnetic field strengths, above 0.5 tesla (T) (5000 gauss); normal operation of the electrographic detector was at field strengths of 18 to 36 mT (180 to 360 gauss). At very high field strengths, the depth of focus of a magnetically focused electron image becomes very large—i.e., the image resolution becomes nearly independent of the photocathode-emulsion separation distance or the exact values of magnetic field strength or accelerating voltage (17). This allows the use of curved photocathodes, which may be shaped to fit the optical focal surfaces of various telescopes or spectrographs, with flat recording emulsions without loss of resolution. This capability was demonstrated by the use of photocathodes deposited on curved windows in the device.

Another development we have pursued is of a new type of semitransparent photocathode, which combines some of the advantages of conventional semitransparent photocathodes and of opaque photocathodes. This involves deposition of the photoemissive substance on the front surface of an electroformed metal mesh having a square hole pattern with 30 to 50% open area and a spacing of 40 to 80 holes/mm (18). As shown in Fig. 13, photoelectrons produced on the front surface of the coated mesh are drawn through the holes by an electric field, then accelerated, and focused as in the case of a conventional semitransparent photocathode. Since no window is required, such a photocathode can be sensitive in the extreme ultraviolet below 1050 Å. Although the quantum efficiency is somewhat less than half that of a conventional opaque photocathode, it still is higher than that of a conventional semitransparent photocathode, even in the wavelength range longward of 1050 Å. The only drawback is that the resolution is limited by the hole spacings of the available meshes to less than about 40 lp/mm. However, the substrate meshes are available in sizes up to 150-mm square, so it is quite easy to make large-format detectors with these meshes which have large numbers of resolvable pixels, despite the relatively low resolution.

We have constructed and tested electrographic detectors with mesh-based photocathodes in a number of configurations, some including microchannel intensification as discussed earlier for the electrographic Schmidt camera. A microchannel-intensified, mesh-photocathode detector was used in an extreme-ultraviolet airglow spectrograph which was operated successfully in a February 1978 rocket flight.

MIDDLE ULTRAVIOLET ELECTROGRAPHIC DETECTORS

Our current development efforts in the NRL Space Science Division are concentrated on the extension of the wavelength range of our electrographic detectors to include the middle-ultraviolet (2000- to 3000-Å) spectral range. This requires the use of cesium telluride (Cs_2Te) photocathodes instead of CsI or other alkali halides. Cs_2Te, like the photocathodes sensitive in the near-visible spectral range, cannot be exposed to air and must be protected from emulsion outgassing in vacuum. Therefore, electrographic detectors for the middle UV are necessarily similar to those used in the near-visible range, which suggests that once our detectors are operational in the middle UV it would be a relatively simple task to extend their range of spectral coverage to include the near-visible range.

We currently are developing two types of middle-UV electrographic detectors, electrographic Schmidt cameras incorporating opaque Cs_2Te photocathodes but otherwise similar to the far-UV electrographic Schmidt cameras, and semitransparent-photocathode detectors, similar to the large-format far-UV detector

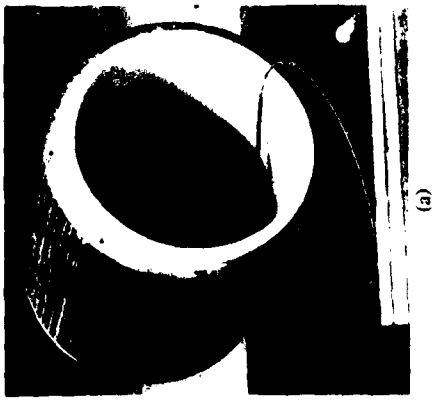

(a)

(b)

(c)

Fig. 12 – Large-format, far-ultraviolet semitransparent-photocathode electrographic detector developed at NRL. Useful image diameter is 123 mm, and the instrument has demonstrated resolution of better than 10 μm over this area: (a) assembled device, (b) disassembled to show components (permanent focusing magnet, insulating liner, film transport assembly, photocathode holder, and accelerating ring assembly), (c) superconducting solenoid, used alternatively in place of the permanent magnet.

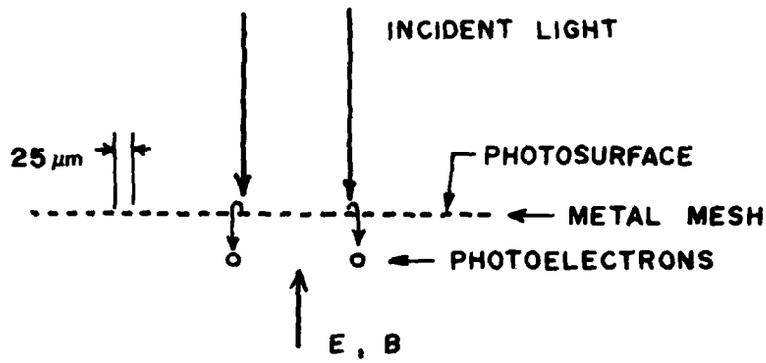

Fig. 13 – The principle of operation of a mesh-based semitransparent photocathode.

described earlier (19). Figures 14 and 15 show diagrams of these detectors. These devices use the barrier-membrane technique, as used in the Griboval detector, for photocathode protection; as part of our program we have developed methods for making polyimide films as thin as 2 μm and as large as 175-mm diameter from commercially available polyimide varnish.

Devices currently undergoing laboratory testing are a 75-mm aperture, f/1.5 electrographic Schmidt camera and a 70-mm image diameter, semitransparent photocathode detector. Planned for construction and testing during the coming year are a 150-mm aperture, f/2 electrographic Schmidt camera, very similar to the large far-UV Schmidt camera currently in use in our sounding rocket program, and a 120-mm image diameter, semitransparent photocathode detector analogous to the 123-mm-image far-UV large format camera currently operational.

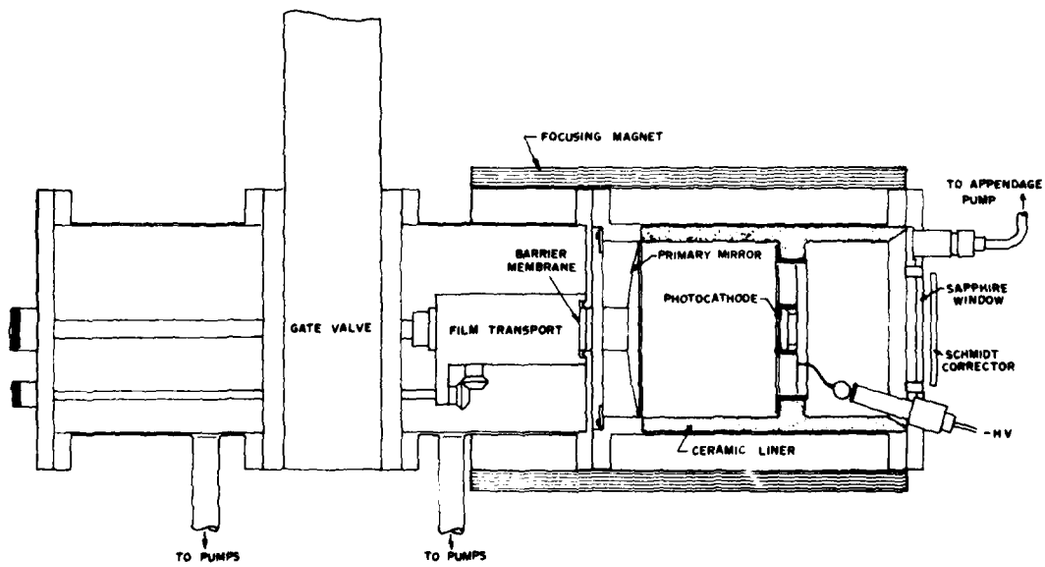

Fig. 14 – Middle-ultraviolet-sensitive electrographic Schmidt camera under development at NRL. This device uses an opaque cesium telluride photocathode, which is protected from emulsion outgassing by a barrier membrane. The membrane is protected from excessive pressure differential during film changes by the gate valve–airlock assembly.

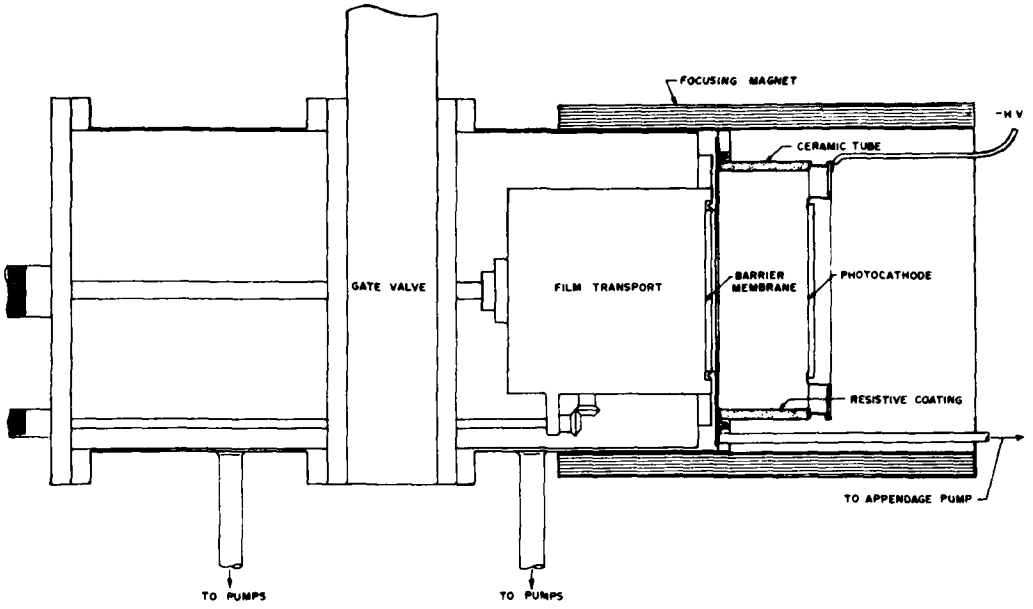

Fig. 15 - Large-format, middle-ultraviolet semitransparent-photocathode electrographic detector under development at NRL. Except for the use of a semitransparent cesium telluride photocathode, the device is basically similar to that in Fig. 14.

TECHNIQUES FOR ANALYSIS OF ELECTROGRAPHIC IMAGES

Electrographic, like photographic, emulsions provide a convenient analog storage medium. However, as discussed earlier, the dynamic range and photometric quality of an electrographic exposure (electrograph) can be far superior to those of a conventional photographic exposure. But what is needed, if the full information content is to be extracted from the recorded image, is a practical means of sampling the stored intensity information which will accommodate large areas of emulsion but at a scale sufficiently small that the inherent image resolution is not seriously degraded. It must also have sufficient dynamic range to record the full useful range of emulsion densities. To allow the intensity information to be further processed and analyzed, this means must convert the information to a form which can be handled by a computer - i.e., the image must be digitized.

Since virtually every photoelectron is recorded in the emulsion as a track, the best method of preserving the photometric integrity of the image would be to count the number of tracks which occur within each elemental picture area. However, the tracks are small (depending on the emulsion, they have characteristic dimensions only a few times larger than the wavelength of visible light) and no machine currently exists to automate the process. Manual counting using a microscope would be a herculean task and hardly represents an efficient means of retrieving the enormous amount of information stored on the emulsion.

A practical method is to scan the recorded image with a microphotometer, or microdensitometer, which measures the relative optical transmission of small areas of the emulsion as a function of position, and to record the output in digital form for subsequent data processing via digital computer. The photomultiplier in such a device introduces unwelcome noise in the process, but potentially more important systematic errors are introduced which may compromise the photometric potential of the electrograph. Three potential sources of error may be all but eliminated by careful attention to the design and use of the microphotometer: drift due to variation in the effective intensity of the analyzing light source during the time it takes to complete a measurement sequence; scattered light, which results in overestimating the

transmission in particularly opaque areas of the emulsion; and lag, which results when the scanning speed exceeds the response time of mechanical and/or electronic components of the microphotometer, and which effectively skews the profile of an image in areas where gradients are steep. Another error arises from the fact that a microphotometer, neglecting other potential sources of error, measures the transmission (T) through a spot projected onto the emulsion, not the optical density (d) which is desired. Transmission and density are related by $d = -\log_{10} T$, but this equation is valid only if the opacity of the emulsion is constant within the spot. In the presence of image gradients, the quantity actually measured by the microphotometer is the *average* transmission, and this is not equivalent to measuring the average density. This leads to an underestimate in the true density and is a principal source of nonlinearity in the digitization process. This error is fundamental, but its effect can be minimized by using a scanning aperture as small as possible and yet consistent with the noise characteristics of the photomultiplier.

Once the image has been converted into digital format and transferred to a storage medium which can be accessed by a digital computer, it becomes practical to transform the image into one of near-uniform photometric quality through the application of instrumental calibrations and various corrections to the recorded data. These transformations can be described by analytic expressions and may involve corrections for photometric nonlinearity, spatial variation of effective sensitivity, or geometric distortion. Photometric nonlinearities may have been introduced by any failure to record all of the emitted photoelectrons, by the recording emulsion itself or the characteristics of the chemical development process, or during the digitization process. The determination of the nature of this correction is particularly easy and accurate for electrographic exposures because a change in source intensity may be simulated simply by a change in exposure time, since there is no reciprocity failure. By comparisons of exposures of different duration made on a source known to be of constant intensity, the character of any nonlinearity may be described and corrections may be made to the digital image array on a pixel by pixel basis. The effective sensitivity of the detector may vary from point to point on the image as a result of positional nonuniformity of the photocathode quantum efficiency and/or the manner in which the photocathode is illuminated—e.g., there may be optical vignetting. These variations may be mapped from exposures made on an extended source of known brightness distribution. For cameras with even moderately large fields of view, the twilight sky or the geocorona, for detectors in near-earth space, can provide a good approximation to a source of uniform intensity. Geometric distortion in the image, caused by either the photon optics or electron optics, may be similarly mapped, using exposures made on a scene whose projected geometry is known. Stars serve as excellent fiducials, and comparison of their cataloged positions with their relative positions as measured in the recorded image allows the nature of the distortion to be characterized. The rectification of the distorted image is accomplished in the computer by numerical stretching and squeezing of the digitized image to achieve correspondence. Removal of the effects of distortion is important, since local variations of image magnification can introduce photometric errors. But image rectification also aids in achieving the precise registration required when co-adding exposures (to reduce the effects of noise, so that the detectivity of faint features is improved) and in measuring the brightness ratio of a source observed at different times or in different spectral regions. A knowledge of image distortion also allows the relative positions of faint, perhaps previously undetected, objects to be specified.

The application of these photometric and geometric corrections simulates the record of a camera consisting of a rectilinear array of identical sensing elements, each having linear response. However, the photometric quality of the image may not be completely uniform, since each picture element has a "noise value" associated with it which depends not only on the nature of the camera/detector/microphotometer, but also on sources of noise in the original scene. The image may be enhanced to some extent by filtering of the digital image, if the sources of noise are understood and if their effects can be adequately modeled. High-spatial-frequency noise, such as that caused by defects in the recording emulsion (dust, pinholes, scratches, etc.), and noise of low spatial frequency, such as that due to a slowly varying background, can be easily and accurately subtracted from an image of a scene with intrinsically moderate spatial frequencies. Enhancement obviously becomes more difficult when the characteristics of noise are similar to those of the object of interest, e.g., when one conducts stellar photometry in crowded fields where neighboring stars

represent a source of noise or when one tries to study low-contrast features in an extended source such as a faint galaxy superimposed on the night sky whose brightness also varies slowly with position. The effects of some sources of noise (for example those due to poor sampling statistics) may be reduced by co-adding images to improve the signal-to-noise ratio or by simply smoothing the digital array at the expense of image resolution.

Many of the calibration, rectification, and enhancement procedures outlined above are similar to those applied to other types of digital imagery. But because of the oftentimes superior sensitivity, resolution, dynamic range, and photometric potential of the electrographic technique, the various calibrations and transformations may be more accurately determined so that results of significantly higher quality are achieved.

To synthesize the numerical data contained in the digital image into forms which are more readily usable, a variety of analysis techniques may be used to extract scientifically useful parameters such as brightnesses, colors, or positions. For example, since the digital array is photometrically linear, the brightness of a star is proportional to the values in the array summed over the area of the star image. Graphical portrayals of the distribution of intensity within the image are used to clarify further the scientific interpretation. For example, plots of image profiles and isophotal contour and isometric plots of the intensity distributions of star fields and extended sources may be generated (see Fig. 16). Likewise, plots of spectral energy distributions may be derived from spectral imagery (Fig. 17). The image may even be reconstructed using a variety of computer peripherals to display the enhanced version with boosted contrast or with quantitative color coding of intensity levels.

SPACE-SCIENCE APPLICATIONS OF ELECTROGRAPHIC DETECTORS

The primary motivation for our development of electrographic detectors has been for their application to our ultraviolet-astronomy program. Since 1966 (20) the electrographic Schmidt cameras and all-reflecting cameras have been used for direct imagery and objective spectrography of star fields in the far-ultraviolet (950- to 2000-Å) spectral range. These investigations, with two exceptions, were carried out from sounding-rocket vehicles, which typically provide about 4 min of observing time above the atmosphere.

Among the scientific results obtained from these rocket flights were the first detection of interstellar molecular hydrogen (21), measurements of interstellar atomic hydrogen in the direction of several stars (22), far-ultraviolet imagery of Comets Kohoutek and West (23-26), and far-ultraviolet imagery of galactic nebulae (27-29) and of the Andromeda Galaxy (30). Results obtained in a flight of an electrographic objective spectrograph have been reported previously (31).

Two missions involving the use of our detectors were of much longer duration than the typical sounding rocket missions; these were the *Apollo 16* mission, in April 1972, and the *Skylab 4* mission, from November 1973 to February 1974. These carried our S201 Far-Ultraviolet Camera, with spectrographic mode on the *Apollo 16* mission (13,32). In the first of these missions, the camera was set up on the lunar surface and used to obtain ultraviolet images and spectra of the earth's upper atmosphere and geocorona (33), the Large Magellanic Cloud (34,35), and several other fields (36). The ultraviolet images were obtained in the wavelength ranges 1050 to 1600 Å and 1250 to 1600 Å, and the spectra covered the 500- to 1600-Å and 1050- to 1600-Å ranges. Ultraviolet imagery was obtained for a total of 10 fields of 20° diameter, covering about 7% of the sky.

In the *Skylab 4* mission the primary objective was to obtain ultraviolet images of Comet Kohoutek at several different times during the mission, which included the comet's closest approach to the sun in December 1973 (37). The camera also was used to obtain images of star fields not observed during the *Apollo 16* mission, as well as of terrestrial atmospheric auroral and airglow emissions.

Our most recent sounding-rocket investigations have been based on the use of the newest version of our electrographic Schmidt camera (150-mm aperture, f/2) in direct imaging and objective spectrographic

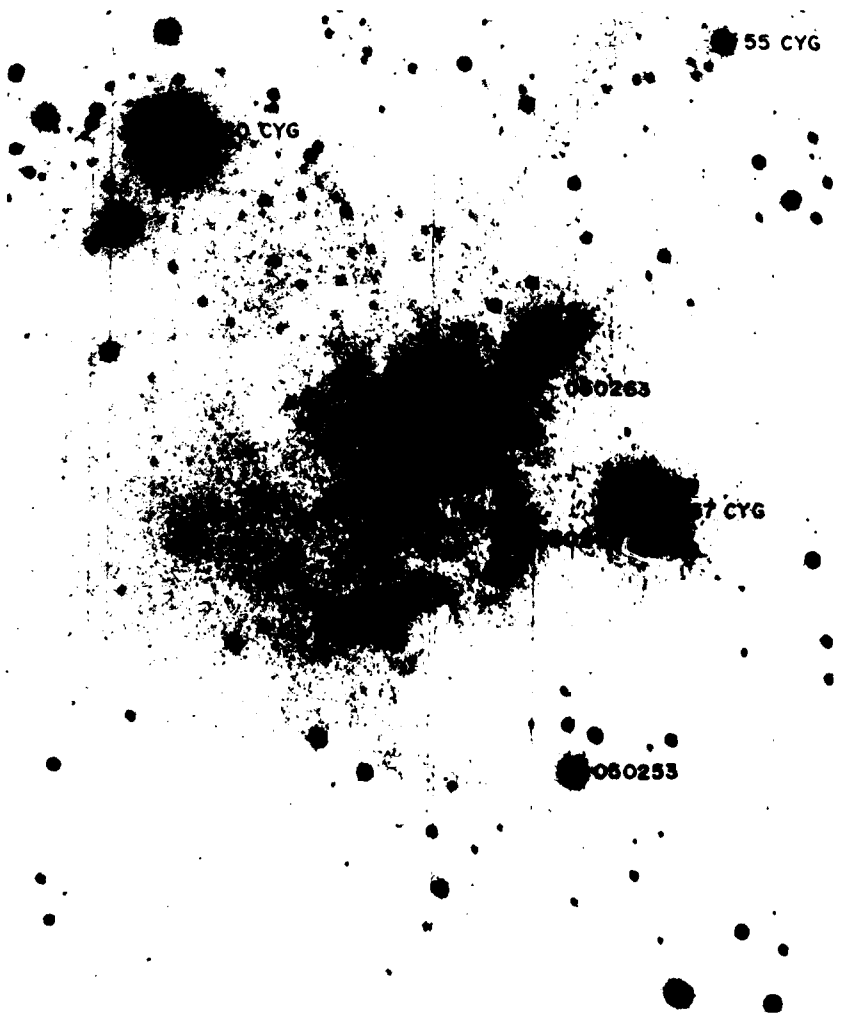

Fig. 16(a) - Far-ultraviolet electrograph of the North America Nebula (wavelength range 1230 to 2000 Å) obtained with the 150-mm aperture, f/2 electrographic Schmidt camera in its first sounding rocket flight (NASA 26.056 DG) 29 October 1976.

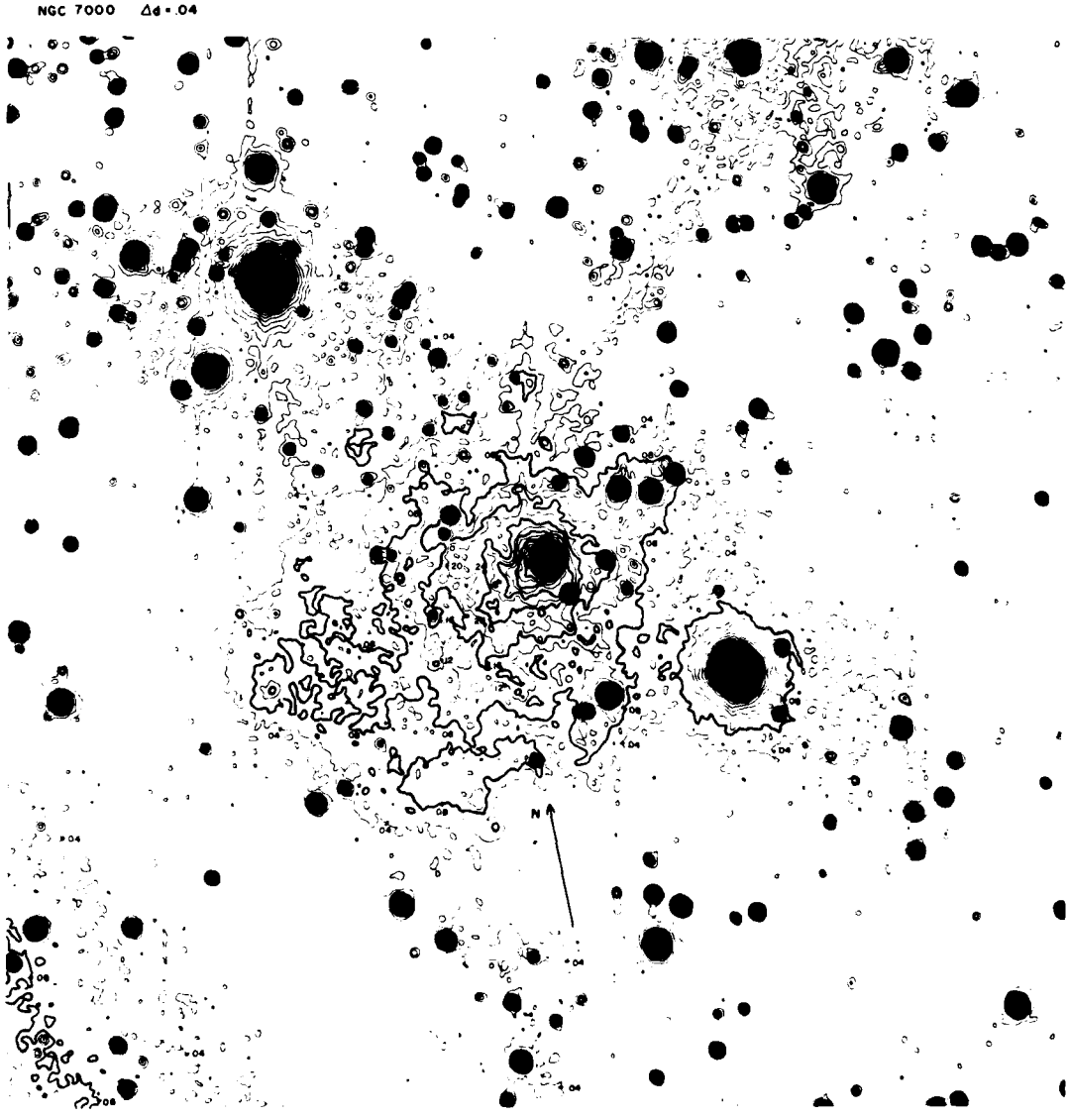

Fig. 16(b) — Isophotal contour plot of th image, obtained by microdensitometry on the Grant machine at NRL followed by computer processing. The numbers denote optical density levels measured; combined with instrument calibrations these yield absolute UV brightness levels.

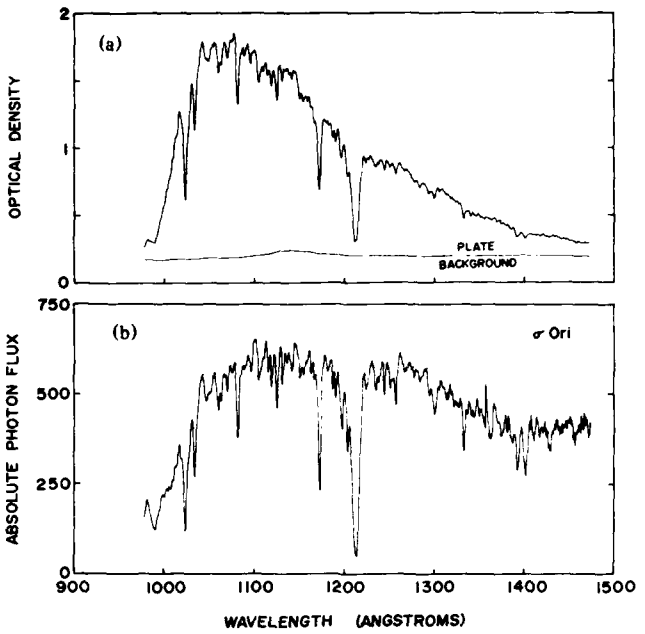

Fig. 17 – (a) Microdensitometer scan of a spectrum of the star σ Orionis, obtained with the all-reflecting objective spectrograph in a sounding rocket flight (NASA 13.118 DG) launched 6 December 1975. The optical density is the average of the three densest pixels (transverse to the spectral dispersion) at each position along the spectrum. (b) Absolute flux distribution, obtained by further computer processing of the spectrum microdensitometry. The contributions of all pixels transverse to the spectral dispersion have been added, and at each point in the spectrum a correction has been applied for each of the following instrumental effects: sensitivity vs wavelength (from preflight calibrations), optical vignetting, and geometrical distortion. Plate background, due principally to geocoronal Lyman-α emission of hydrogen (plotted above), has also been subtracted.

modes, and of a new nebular spectrograph based on the microchannel-intensified electrographic Schmidt camera.

In a flight in October 1976, the large Schmidt camera was used to obtain imagery of the Andromeda Galaxy and of the North America Nebula in Cygnus, covering the 1230- to 2000-Å wavelength range (see Fig. 16). In a May 1978 flight an objective grating was used with an annular aperture in place of the Schmidt corrector to obtain spectra of stars in an 11°-diameter field in Cygnus over the 950- to 2000-Å wavelength range with about 3-Å spectral resolution (38). Preflight calibration of the instrument was done using the National Bureau of Standards SURF II synchrotron storage ring light source as a standard, allowing the absolute spectral energy distributions of the observed stars to be more accurately determined. The cylindrical bar-magnet array used to provide the focusing field in the first two flights provided less than satisfactory field uniformity, but this has now been replaced with a new high-uniformity permanent-magnet focusing assembly obtained from the Raytheon Corporation. The camera is now undergoing laboratory tests with the new magnet, and further flights on sounding rockets and/or the space shuttle are being proposed.

Our ultimate goal in flights of the instrument on the shuttle would be to perform an all-sky ultraviolet survey in both direct-imaging and objective-spectrographic modes. In 20-min exposures we estimate

that useful imagery of stars as faint as 19th visual magnitude could be obtained, and that useful spectra at 2-Å resolution of 11th magnitude stars could be acquired. In addition, imagery of diffuse nebulae and galaxies to much fainter limits than possible from sounding rockets could be obtained.

The nebular spectrograph (Fig. 18) is a slit-type spectrograph intended for more detailed studies of diffuse sources than is possible with an objective-grating (slitless) spectrograph. This instrument was flown for the first time in June 1979 to observe the North America Nebula and the Cygnus Loop Nebula. The wavelength range of the instrument is 1050 to 2000 Å and the spectral resolution about 5 Å. The use of f/1 Schmidt optics, an opaque photocathode, and microchannel intensification gives this instrument exceptionally high sensitivity in spectrography of diffuse sources. Future sounding-rocket flights are planned for studies of diffuse nebulae and comets, and a modification of the instrument for shuttle flights has been proposed.

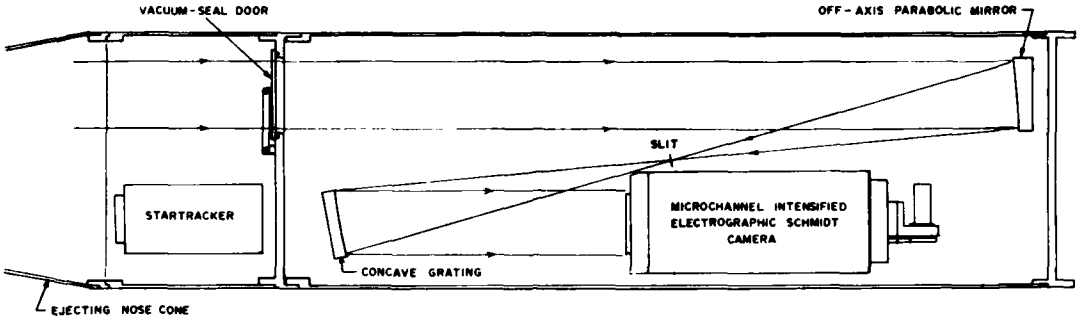

Fig. 18 – Nebular spectrograph in use in sounding rocket flights by NRL. A microchannel intensified electrographic Schmidt camera, shown in Fig. 10, is used as the detector.

In addition to our far-UV astronomy program, we are undertaking spectral observations of terrestrial airglow and auroral emissions, particularly in the wavelength range 500 to 1000 Å, with higher spectral resolution than has been achievable in previous observations. For this purpose we are using a mesh-photocathode detector with microchannel intensification (Fig. 19), which records the dispersed spectrum produced by a concave grating and entrance slit. An earlier version of this instrument was used for observations of the day airglow in the 500- to 1300-Å range in a February 1978 rocket flight; the spectral resolution achieved was about 2 Å. A higher-resolution version of this instrument is under development; it will

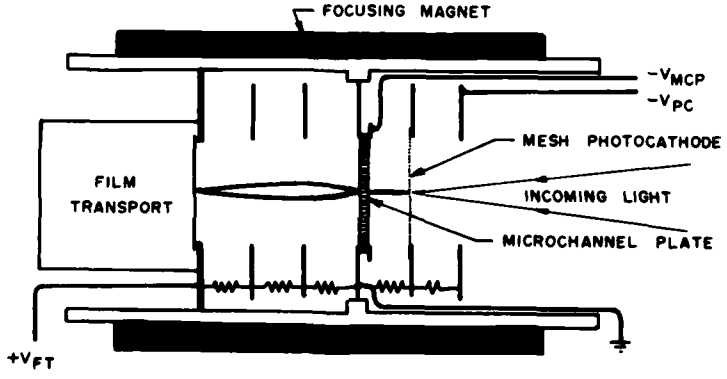

Fig. 19 – Electrographic detector using a mesh-based semitransparent photocathode and microchannel intensification. This detector is used in an extreme-ultraviolet auroral/airglow spectrograph developed and used in sounding rocket flights by NRL.

cover the 500- to 1000-Å and 900- to 1400-Å ranges, using two gratings and a single detector, with about 0.8-Å resolution. It is planned for observations of day airglow and of a proton aurora.

The middle-ultraviolet-sensitive detectors currently under development will extend the wavelength range of coverage by our instruments to include the entire ultraviolet range up to 3200 Å. (The earth's armosphere limits ground-based observations to the range longward of 3000 Å; hence, the middle-UV instruments will provide overlap between space- and ground-based observations.) The middle-UV range is of particular importance for the study of interstellar dust, as there is a characteristic absorption feature or "bump" near 2200 Å, which is believed to be due to graphite particles in interstellar dust (see Fig. 20).

Further extension of the wavelength range of our detectors will also make them useful for ground-based astronomy. The electrographic Schmidt camera, in particular, will be useful for wide-field surveys using various photometric or narrow-band emission line filters or using an objective prism or grating. At present, we are using a Kron electrographic camera in just this fashion; this camera, on loan to NRL from the NASA Johnson Space Center, is set up at McDonald Observatory at Ft. Davis, Texas (see Fig. 21) with a Questar 178-mm aperture, f/2.8 telescope. It is used in support of our ultraviolet and x-ray astronomy

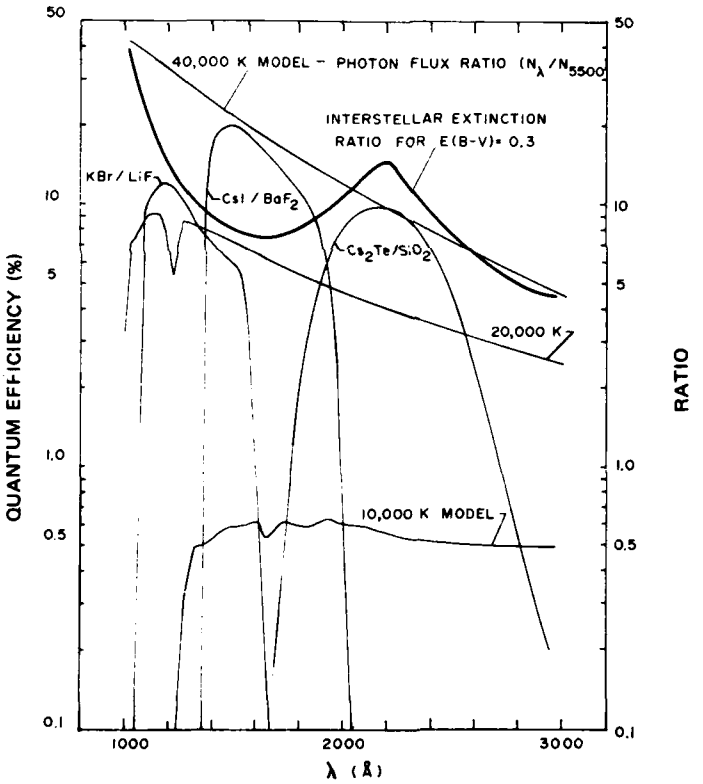

Fig. 20 – Typical spectral responses of electrographic Schmidt cameras, including one sensitive in the middle ultraviolet, along with relative photon flux distributions of theoretical high-temperature stellar atmospheres (40), and a typical curve of the extinction vs wavelength due to interstellar dust (41). Note that the middle-UV camera allows measurements near the peak of the interstellar extinction at 2200 A. Sky surveys with a "three-color" instrument package will allow the effects of interstellar extinction and of stellar temperature to be separated and independently determined.

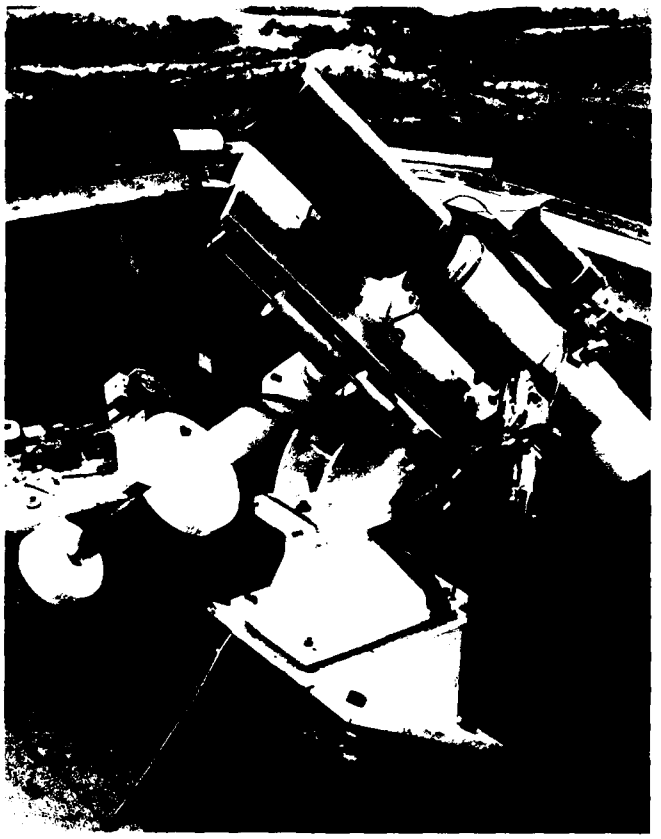

Fig. 21 — Kron electrographic camera and Questar telescope in use by NRL at the McDonald Observatory in Texas, for narrow-band imagery of diffuse nebulae.

programs, and its photometric and dynamic-range superiority over image intensifier/photographic recording techniques has been well demonstrated (19,39) (see Fig. 22). The electrographic Schmidt could also be used as an integral camera/detector in conjunction with spectrographs designed to be used at the prime or cassegrain focus of large reflecting telescopes.

LABORATORY AND OTHER APPLICATIONS OF ELECTROGRAPHIC DETECTORS

In addition to our uses of electrographic detectors in space science, there are numerous other present and potential applications of these detectors in other fields. For example, we are using electrographic Schmidt cameras in collaboration with the U.S. Air Force for studies of far-ultraviolet emissions from rocket exhaust plumes, both in ground-based vacuum-test chambers and in sounding-rocket flights. Our investigations so far have mainly been of direct imagery of these sources, but we expect that our nebular spectrograph will also be useful in future studies. Far-ultraviolet observations of military interest will be combined with basic research objectives in use of an instrument package we are preparing for a space-shuttle flight opportunity to be provided by the USAF Space Test Program. The payload consists of two

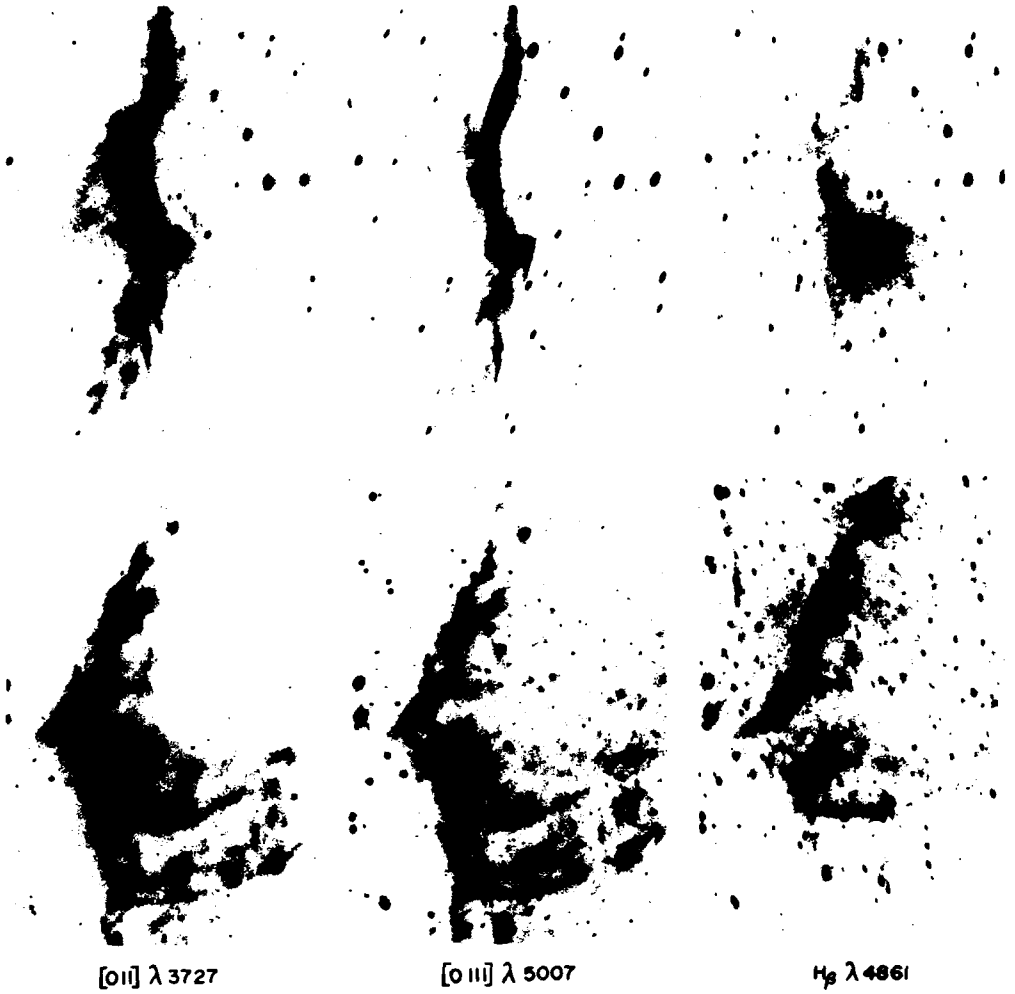

Fig. 22 – Example of electrographic imagery obtained with the instrument of Fig. 21. Shown are (top) the eastern portion, and (bottom) the western portion of the Cygnus Loop Supernova Remnant, taken in the wavelengths of three nebular emission lines. Wider-field, but lower-resolution, imagery taken with the Kron camera and a shorter focal length lens are discussed in Refs. 19 and 39.

electrographic Schmidt cameras, covering the 1050- to 1600-Å and 1230- to 2000-Å wavelength ranges, mounted on a pointing platform to be installed in the shuttle payload bay. Middle-UV-sensitive electrographic Schmidt cameras have potential applications of military interest in ground-level and low-altitude observations.

Electrographic detectors have many potential applications to spectrography and photometric-quality imagery in laboratory investigations such as plasma-physics experiments. Our nebular spectrograph and airglow spectrograph are readily adaptable to laboratory use, as are the smaller versions of the electrographic Schmidt camera. Large-format, visible-light-sensitive electrographic cameras have potential future applications to aerial and satellite mapping, reconnaissance, and earth-resources studies.

In each case, the advantage of electrographic detectors over conventional image-intensifier/film combinations is the much-better photometric quality and the higher achievable resolution. The advantage over television-type sensors, as in astronomy, is that film offers a much-simpler and more-compact method of storing very large quantities of information than do combinations of video sensors, telemetry systems and/or data-storage media such as magnetic tape. In satellite applications, the rate of data acquisition by electronic-readout imaging sensors is almost always limited by the telemetry link and/or data-storage facility; such limitations are not encountered with electrographic imagery.

REFERENCES

1. M. Cohen and E. Kahan, in *Advances in Electronics and Electron Physics*, Vol 33A, p. 53 (Academic Press, New York, 1972).
2. P. Griboval, D. Griboval. M. Marin, and J. Martinez, in *Advances in Electronics and Electron Physics*, Vol. 33A, p. 67 (Academic Press, New York, 1972).
3. R. W. Decker, in *Advances in Electronics and Electron Physics*, Vol. 28A, p. 357 (Academic Press, New York, 1969).
4. A. Lallemand, *C. R. Acad. Sci. Paris* **203**:243, 990 (1936).
5. A. Lallemand and M. Duchesne, *C. R. Acad. Sci. Paris* **233**:305 (1951).
6. A. Lallemand, M. Duchesne, and G. Wlerick, in *Advances in Electronics and Electron Physics*, Vol. 12, p. 5 (Academic Press, New York, 1960).
7. G. E. Kron, H. D. Ables, and A. V. Hewitt, in *Advances in Electronics and Electron Physics*, Vol. 28A, p. 1 (Academic Press, New York, 1969).
8. J. D. McGee, A. Khogali, A. Ganson, and W. A. Baum, in *Advances in Electronics and Electron Physics*, Vol. 22A, p. 11 (Academic Press, New York, 1966).
9. D. McMullan, J. R. Powell, and N. A. Curtis, in *Advances in Electronics and Electron Physics*, Vol. 33A, p. 37 (Academic Press, New York, 1972).
10. P. J. Griboval, in *Instrumentation in Astronomy-III* (Vol. 172 of Proceedings, Society of Photo-Optical Instrumentation Engineers), p. 348 (1979).
11. G. R. Carruthers, *Appl. Opt.* **8**:633 (1969).
12. G. R. Carruthers and C. B. Opal, in *Instrumentation in Astronomy* (Vol. 28 of Proceedings, Society of Photo-Optical Instrumentation Engineers), p. 203 (1972).
13. G. R. Carruthers, *Appl. Opt.* **12**:2501 (1973).
14. G. R. Carruthers, in *Instrumentation in Astronomy-III* (Vol. 172 of Proceedings, Society of Photo-Optical Instrumentation Engineers), p. 304 (1979).
15. G. R. Carruthers, J. Kervitsky, and C. B. Opal, in *Advances in Electronics and Electron Physics*, Vol. 40A, p. 91 (Academic Press, New York, 1976).
16. G. R. Carruthers, presented at Seventh Symposium on Photoelectronic Image Devices, Imperial College, London (1978).
17. J. P. Picat, *Astron. Astrophys.* **11**:257 (1971).
18. G. R. Carruthers, *Appl. Opt.* **14**:1667 (1975).
19. H. M. Heckathorn, G. R. Carruthers, and S. D. Shulman, in *Instrumentation in Astronomy-III* (Vol. 172 of Proceedings, Society of Photo-Optical Instrumentation Engineers), p. 292 (1979).
20. G. R. Carruthers, *Rept. NRL Prog.* July 1966, p. 7.
21. G. R. Carruthers, *Astrophys. J. Lett.* **161**:L81 (1970).
22. G. R. Carruthers, *Astrophys. J. Lett.* **156**:L97 (1969).
23. C. B. Opal, G. R. Carruthers, R. R. Meier, and D. K. Prinz, *Science* **185**:702 (1974).
24. R. R. Meier, C. B. Opal, H. U. Keller, T. L. Page, and G. R. Carruthers, *Astron. Astrophys.* **52**:283 (1976).
25. C. B. Opal and G. R. Carruthers, *Astrophys. J.* **211**:294 (1977).
26. C. B. Opal and G. R. Carruthers, *Icarus* **31**:503 (1977).
27. G. R. Carruthers and C. B. Opal, *Astrophys. J. Lett.* **212**:L27 (1977).
28. G. R. Carruthers and C. B. Opal, *Astrophys J.* **217**:95 (1977).
29. G. R. Carruthers, H. M. Heckathorn, and T. R. Gull, *Astrophys. J.*, accepted for publication (1980).
30. G. R. Carruthers, H. M. Heckathorn, and C. B. Opal, *Astrophy. J.* **225**:346 (1978).
31. G. R. Carruthers, C. B. Opal, and H. M. Heckathorn, *Rept. NRL Prog.* Oct. 1978, pp. 1-25.
32. G. R. Carruthers and T. Page, Chap. 13 in *Apollo 16 Preliminary Science Report*, NASA SP-315 (National Aeronautics and Space Administration, 1972).
33. G. R. Carruthers and T. Page, *Science* **177**:788 (1972).
34. G. R. Carruthers and T. Page, *Astrophys. J.* **211**:728 (1977).
35. T. Page and G. R. Carruthers, "S201 Far-Ultraviolet Atlas of the Large Magellanic Cloud," NRL Report 8206 (1978).

36. T. Page, G. R. Carruthers, and R. Hill, "S201 Catalog of Far-Ultraviolet Objects," NRL Report 8173 (1978).
37. T. Page, in *Proceedings of AIAA/AGU Conference on Scientific Experiment of Skylab* (AIAA, New York), p. 265 (1976).
38. G. R. Carruthers, H. M. Heckathorn, and C. B. Opal, *1978 Review* (Naval Research Laboratory, Washington, 1979), pp. 130-133.
39. H. M. Heckathorn and S. D. Shulman, *1978 Review* (Naval Research Laboratory, Washington, 1979), pp. 133-135.
40. R. L. Kurucz, E. Peytremann, and E. A. Avrett, *Blanketed Model Atmospheres for Early-Type Stars* (Smithsonian Press, Washington, 1974).
41. R. C. Bless and B. D. Savage, *Astrophys J.* 171:293 (1972).

GEORGE R. CARRUTHERS did his undergraduate and graduate work at the University of Illinois, receiving his Ph.D. in 1964. Since then he has been with the E. O. Hulburt Center for Space Research, working in ultraviolet space astronomy and ultraviolet studies of the upper atmosphere, and in the development of electronic imaging devices. He was Principal Investigator for the Apollo 16 Far-Ultraviolet Camera/Spectrograph experiment, and co-investigator for the Skylab 4 and sounding rocket experiments which obtained ultraviolet images and spectra of Comet Kohoutek. He is currently Head of the Ultra-Violet Astronomy Section.

HARRY M. HECKATHORN did his undergraduate work at Carleton College and received his M.S. and Ph.D. degrees in Astronomy at Northwestern University in 1970. His experience has been in the areas of observational astrophysics, astronomical instrumentation, space astronomy, and in the development and use of electrographic imaging devices for astronomical applications. His postdoctoral work was done at NASA's Johnson Space Center where he was an NRC research associate. Since then, he has held positions as an astronomer in the Physics Department of the University of Houston, with Lockheed Electronics Co., and with the Physics Department of the Johns Hopkins University. He has recently received a career appointment in the Space Science Division of NRL.

PROGRESS NOTES

These brief reports describe significant, unclassified, technical progress on some of the projects or problems of NRL's research and development program. The reports are arranged according to the field of research, with sponsor and NRL problem number given at the end of each.

CHEMISTRY

Effect of Loading Rate on the Fracture Energy of A Toughened Epoxy Polymer

R. Y. Ting, *Chemistry Division*

Background: Epoxy polymers are used widely as matrix materials for fiber-reinforced composites. For such applications polymer fracture properties are of great importance because the composite failure mechanism is generally dominated by crack propagation, resulting from the growth of flaws and microvoids inherently present because of the processing techniques employed in fabricating organic-matrix composites. To mitigate the brittleness of epoxy matrix resins, it is a common industrial practice to add elastomers to the epoxy resin for copolymerization and formation of a uniformly dispersed phase of small rubber particles. These particles have been demonstrated to enhance the toughness of unmodified epoxy (1).

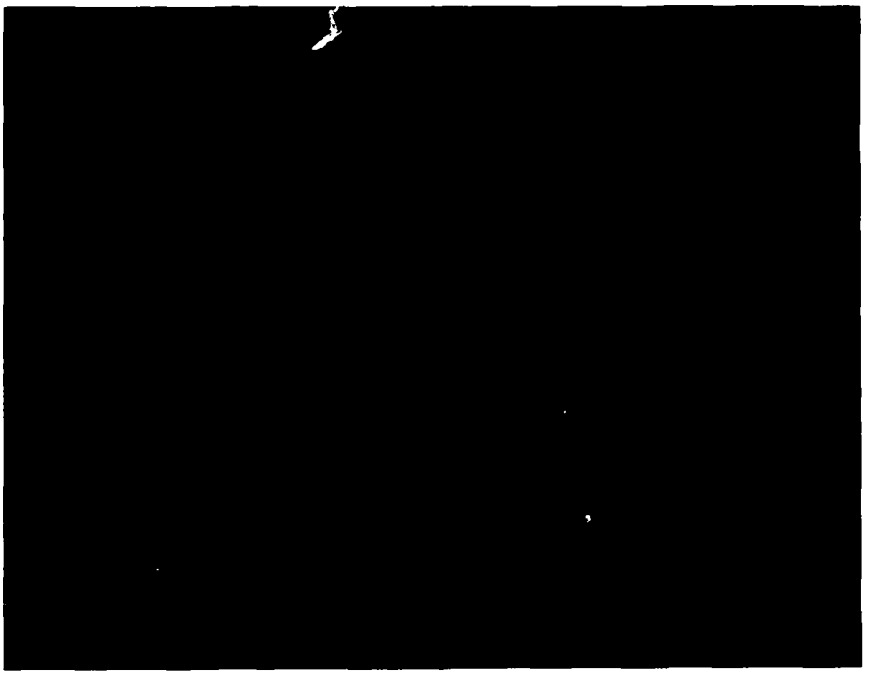

Fig. 1 Record of impact load and energy vs impact time. Time increases from left to right at a scale of 0.5 m-s per division.

Progress: Recently the Hexcel Corporation (of Dublin, California) developed a model epoxy system having a bimodal distribution of carboxy-terminated butadiene acrynitrile (CTBN) particle sizes, peaking at about 3 to 5 μm and 10 to 20 μm in diameter. The fracture behavior of this modified epoxy polymer has been studied at NRL. Compact tension specimens were prepared and the fracture energies determined from INSTRON measurements at varying crosshead speeds. Standard Izod impact tests, representing a high-loading-rate case, were also carried out. Figure 1 shows the typical data with impact load and energy recorded as functions of impact time. The impact data were used to derive the sample fracture energy based on theories of linear elastic fracture mechanics (2).

In Fig. 2 polymer fracture energy G_c is shown as a function of the loading rate. It is clear that the elastomeric inclusions greatly increased the fracture energy of the base epoxy. At the lowest rate tested, this toughening effect is manifested by an increase in G_c by as much as a factor of 30. The presence of large particles (10 to 20 μm) seemed to have introduced further increase in fracture energy over that attained with small CTBN particles (3 to 5 μm) alone (1). However, the improved G_c value for the modified epoxy system was also found to decrease rapidly with increasing loading rate. At very high loading rates, the fracture energy of the toughened polymer levels off to a value only about eight times that of the base epoxy. This rate-dependent fracture energy of a rubber-toughened epoxy is important: for high loading-rate applications, such as in impact failure, the toughening effect of elastomers on brittle epoxies becomes less impressive.

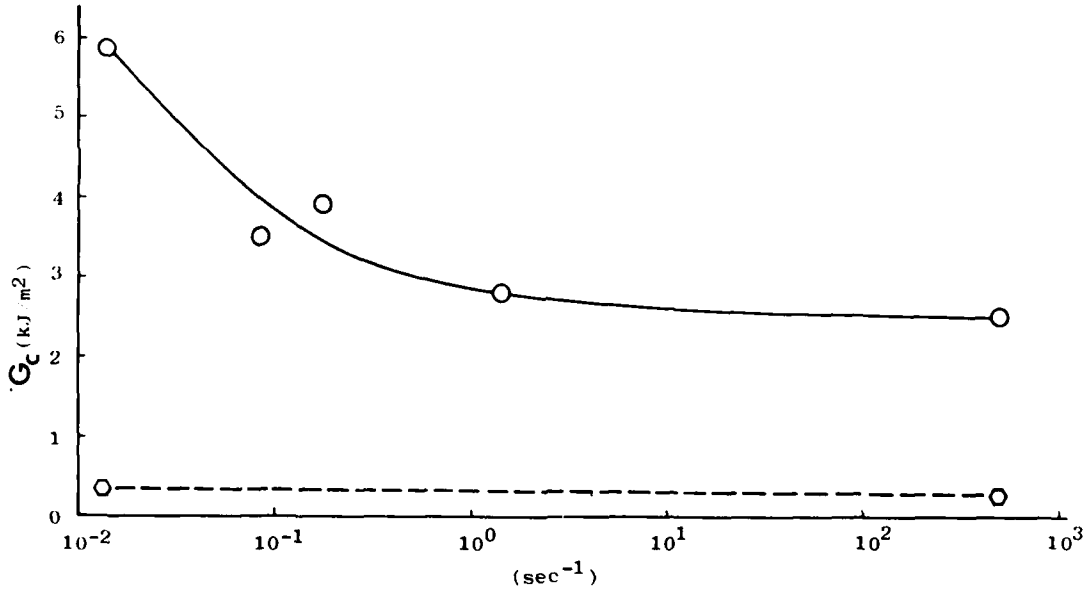

Fig. 2 – Polymer fracture energy as a function of loading rate. The solid line is for the modified epoxy, and the dotted line for the unmodified base epoxy.

REFERENCES

1. W. D. Bascom and R. L. Cottington, *J. Adhesion* 7:333 (1976).
2. P. E. Reed, in *Developments in Polymer Fracture-1*, ed. E. H. Andrews, Applied Science Pub., London, 1979, p. 121.

Sponsor: ONR – NRL Problem No: 0016-0

ELECTRO-OPTICAL TECHNOLOGY

Passive Infrared Surveillance, Part II: Threshold Crossing Receivers

R. A. Steinberg, *Electro-Optical Technology Program Office*

Background: Infrared search and track (IRST) systems are potentially of great use to the Navy for detecting and tracking aircraft and missiles. The IRST designer's task is to devise a signal-processing scheme that will reliably discriminate between real targets and bogus targets having their origin in the natural background scene. This task is complicated in that previous works describing analysis techniques for IRST systems are valid for only spatially uniform scenes. A new IRST analysis method is needed that is inherently applicable to nonuniform scenes.

Progress: An interim report on the problem is being published as NRL Report 8367, "Passive Infrared Surveillance, Part II: Threshold Crossing Receivers," by R. A. Steinberg.

Abstract: A number of infrared passive surveillance receivers are analyzed with the theory developed in Part I (NRL Report 8320). The specific problem of interest is the detection of low-contrast point-source targets against high-contrast structured backgrounds. A new and promising approach to signal processing is proposed for minimizing background-induced false alarms while retaining maximum target detection sensitivity.

It is shown that improvements in focal-plane-array (FPA) technology employing time delay and integration (TDI) may afford "excess" detector sensitivity that we can intentionally sacrifice in the interest of enhanced performance against structured scenes.

Sponsor: CNM — NRL Problem No: N01-29

MATERIAL SCIENCE AND TECHNOLOGY

Cooperative Radiation Effects Simulation Program Annual Progress Report for the Period 1 September 1977–31 August 1978

F. A. Smidt, Jr., *Material Science and Technology Division*
L. A. Beach, *Radiation Technology Division*

Background: The Cooperative Radiation Effects Simulation Program (CORES) was initiated voluntarily by five Branches from the Engineering Materials Division (now the Material Science and Technology Division) and the Radiation Technology Division of NRL on the basis of their common interests in the problems of simulating radiation damage in metals. The program promotes the exchange of information, discussion of problems, and the pursuit of collaborative research efforts. Annually a written report is prepared containing those portions of the work of the participating Branches which are judged to be of interest to the damage simulation problem. The major portion of the work is sponsored by the Office of Naval Research. Since research findings which apply to the objectives of one sponsor may also be of interest to others, the overall progress related to damage simulation is included in the written report. Several of the participating Branches have independent programs on other aspects of the radiation damage problem; when results obtained in these programs are judged to be of interest to CORES participants they may also be included, informally, in the CORES program review.

Progress: A progress report on the problem has been published as NRL Memorandum Report 4080, "Cooperative Radiation Effects Simulation Program, Annual Progress Report for the Period 1 September 1977–31 August 1978," by F. A. Smidt, Jr., and L. A. Beach, dated Oct. 4, 1979. AD-A075 608.

Abstract: The Cooperative Radiation Effects Simulation Program (CORES) is a collaborative effort of the Material Science and Technology and Radiation Technology Divisions of NRL Material and Radiation

Science and Technology Area. The goal of the research is to provide the theoretical and experimental bases for understanding the mechanisms of nuclear radiation damage of metals, as well as a theoretical insight into energy deposition processes. In this the Van de Graaff and Cyclotron are used to simulate rapidly the radiation damage produced over long periods in reactor neutron environments.

Progress for the period 1 September 1977 to 31 August 1978 includes: (1) development of a method for calculating energy-deposition profiles from range distributions; (2) development of a method to estimate energy deposition in ion bombardments which incorporate transport of energy downstream by primary knockon atoms; (3) an investigation of the influence of 1 at.% Al, Mo, Si, and Ti to the swelling behavior of binary nickel alloys under neutron irradiation; (4) an investigation of swelling in refractory metals and alloys (Mo, Nb, V, TZM, Nb-1% Zr, and V-20% Ti) at 625°C for fast-neutron fluences to 5.4×10^{22} n/cm^2; and (5) an investigation of deuterium trapping in radiation-damaged aluminum and stainless steel using elastic-scattering techniques to measure the increase in dislocation density produced by radiation damage in copper single crystals.

Sponsor: ONR – NRL Problem Nos: M01-22, M01-27, H01-83, H01-70, and H01-67

* * * * *

The Effect of Thermal Cycling on the Propagation of a Stress-Corrosion Crack in High-Strength Steel Weld Metal

F. W. Fraser, *Material Science and Technology Division*

Background: The resistance of steel weld metal to stress-corrosion cracking (SCC) depends on the susceptibility of the microstructure. Due to thermal cycling during welding, the as-deposited weld metal undergoes a range of heat treatments, which result in variations in the microstructure, from the root pass area outward to the surface of the weldment.

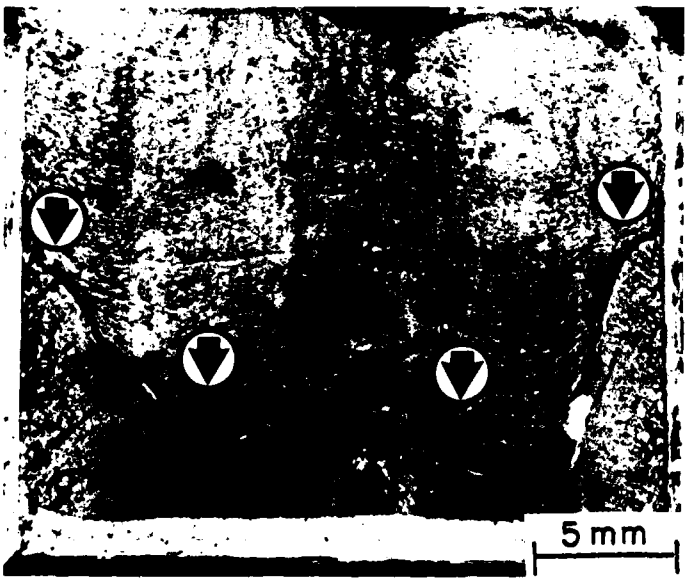

Fig. 1 – Fracture surface of the GTA weldment (arrows indicate the stress-corrosion crack front)

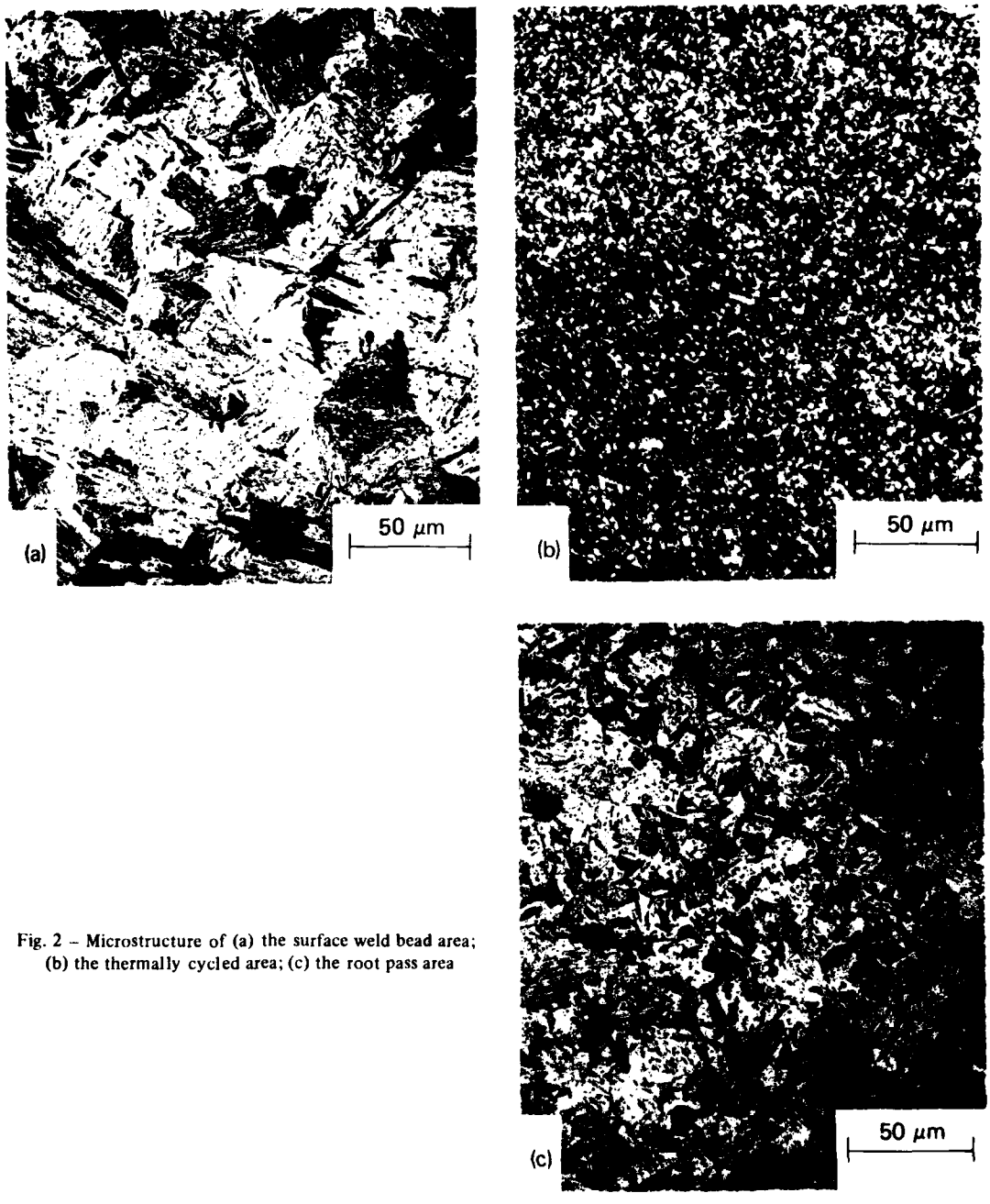

Fig. 2 – Microstructure of (a) the surface weld bead area; (b) the thermally cycled area; (c) the root pass area

Progress: Microstructural and fractographic analyses were carried out on a GTA weldment of HY-130 steel tested for SCC resistance in a 3.5% NaCl solution while galvanically coupled to Zn (1). After preliminary macroscopic examination, the microfracture processes were identified by scanning electron microscopy (SEM). The specimen was then sectioned transversely through the SCC zone and the microstructure was identified optically.

The fracture surface (Fig. 1) shows that the stress-corrosion crack propagated at a nonuniform rate through the weld metal. The arrows indicate the location of the crack front. The rough, coarse fracture on the surface, near the center of the specimen in the root pass area, coincides with a slight bulge indicating accelerated propagation of the stress-corrosion crack. In the adjacent areas, which are smooth and relatively flat, crack propagation was retarded. At the sides of the specimen, in the surface-bead areas, the fracture surface is again rough and coarse textured, and extension of the crack front indicates rapid crack propagation in these locations.

Figure 2 compares the microstructure within the three areas described above. In the final passes during fabrication of the weldment, the surface beads underwent essentially no thermal cycling, and a coarse-grained, untempered microstructure developed (Fig. 2a). Subsequent exposure of this area to the corrosive environment during SCC testing resulted in embrittlement, and fracture occurred by cleavage. The crack front advanced more rapidly in this area than in most of the remaining weld metal, which was subjected to repeated thermal cycling, thereby refining and tempering the microstructure (Fig. 2b). Fracture in the thermally cycled area occurred exclusively by microvoid coalescence (MVC). In the root-pass area the extent of thermal cycling was minimal. The microstructure, although finer than that of the surface-bead area, was still relatively coarse and had undergone little tempering (Fig. 2c). Fracture of the root pass occurred by cleavage and MVC.

Lack of reheating of the surface-weld beads makes them highly susceptible to SCC, as evidenced by an untempered microstructure and low-energy-cleavage fracture. Reheating or thermal cycling of the weld metal results in a refined, tempered microstructure which is beneficial to SCC performance. Effective thermal cycling is difficult to attain in the root-pass area of a double-V weldment, and a coarse-grained microstructure that undergoes relatively little tempering and exhibits various degrees of low-energy fracture results.

Thus, the rate at which a stress-corrosion crack propagates through as-deposited weld metal depends on the degree of tempering and refinement of the microstructure which, in turn, is directly related to the degree of thermal cycling of the weld metal deposited during fabrication of the weldment.

REFERENCES

1. C. T. Fujii, F. W. Fraser, and E. A. Metzbower, "Stress-Corrosion Cracking Characterization of High-Strength Steels–Base Metal and Weldments," NRL Report 8230, May 1978.

Sponsor: ONR – NRL Problem No: 1015-0

* * * * *

Fatigue-Crack Growth of A508 Steel in High-Temperature Pressurized Reactor-Grade Water

W. H. Cullen, Jr., V. Provenzano, H. E. Watson, and F. J. Loss, *Material Science and Technology Division*
K. J. Torronen, *Technical Research Centre of Finland*

Background: The American Society of Mechanical Engineers (ASME) Boiler and Pressure Vessel Code–Section XI contains information on the fatigue-crack growth rate (*da/dN*) upper limits allowed in certain nuclear-reactor safety-related computations. These upper limits are given in the form of two *da/dN* vs ΔK (applied cyclic stress intensity factor) relationships. One of these relationships is appropriate to the case of fatigue-crack growth in an air environment, the other to the case of the high-temperature pressurized reactor-grade water environment. In the safety analysis of Section XI, these *da/dN* vs ΔK relationships are employed in lieu of actual data from the steels used in construction of that particular reactor pressure vessel (RPV) for which the safety analysis is being carried out.

To investigate the validity and conservative nature of the ASME Section XI procedures, research is being conducted to show that commonly used RPV steels do not exhibit corrosion-fatigue crack growth

rates which exceed the Sec. XI guidelines. This involves performing tests in an environment which models that of the primary coolant in the nuclear systems, using materials produced according to accepted practice for the nuclear industry. To address this concern, the Nuclear Regulatory Commission (NRC), together with the Naval Research Laboratory (NRL) and Westinghouse Nuclear Energy Systems developed in 1976 a preliminary test matrix, setting down combinations of waveforms and test temperatures which have now been tested. Data obtained from this program was used to develop a second test matrix encompassing a wide range of materials but only the two waveforms which consistently produced the highest crack growth rates of the preliminary matrix results.

One of the intents of the preliminary matrix was to delineate the effects of rise time and hold time within the loading pattern, and therefore, the waveforms of the preliminary matrix scheme were composed of ramp times ranging from 1 s to 30 min and hold times ranging from essentially zero (reset) to 60 min. Additionally, a 1 cycle per min sinewave test was run to support the proposed conclusions. For all tests at NRL, the load ratio was either 0.1 or 0.125. The two test temperatures of the matrix were 93°C (200°F) and 288°C (550°F). These selections were made because they spanned the characteristics expected during the heatup/cooldown cycle and the hydro- and leak-test transients. To provide uniformity to the results, the same material (A508-2) was used in all of these tests, and the environment was carefully monitored and regulated.

While the crack-growth-rate data were being developed, post-test examination of the fatigue fracture surfaces yielded information on the mechanistic processes responsible for the growth-rate behavior observed. Toward the concluding months of the study, as the significance of the observations began to cohere, a more intensified effort to understand the mechanistic processes resulted in a redoubled metallographic and fractographic effort. The end result is this report, containing descriptions of the techniques used in high-temperature pressurized-water fatigue-crack growth rate testing, a large volume of data, and some observations on the characteristics of that data. These observations are supported by a model involving hydrogen embrittlement, including effects of temperature, rise time and hold time on the hydrogen specie behavior. This model is in turn supported by fractographic observations on selected fatigue fracture surfaces which demonstrate fractographic features characteristic of known hydrogen embrittlement assisted failure.

Progress: An interim report on the problem has been published as NRL Memorandum Report 4063 (NUREG/CR 0969), "Fatigue Crack Growth of A508 Steel in High-Temperature, Pressurized Reactor Grade Water," by W. H. Cullen, Jr., V. Provenzano, K. J. Torronen, H. E. Watson, and F. J. Loss, dated Sept. 29, 1979. AD-A075 506.

Abstract: Fatigue crack growth tests of A508-2 pressure vessel steel have been conducted at two test temperatures (93°C and 288°C) using a variety of constant amplitude waveforms. The load ratios were either 0.1 or 0.125, and the water chemistry was carefully monitored and controlled so as to simulate the nominal pressurized water reactor chemistry. The test procedures are described, and an examination of all the data indicates that the results fall into one of two rather clearly defined categories. One band of data, termed "low," lies close to or essentially on the ASME Section XI Code air environment default line. The other band of data, termed "high," resides approximately midway between the ASME Sec. XI air and water environment default lines. The two bands of data are the result of certain combinations of the waveform and temperature variables listed above, and are determined by the following rules: (1) A ramp time in excess of 1 s is needed to obtain the high crack-growth rate. (2) The application of a hold time, together with a high temperature, serves to depress a normally high crack-growth-rate test (i.e., one with a long ramp time) and force it into the low category.

A hydrogen embrittlement model is used as a basis for the explanation of this behavior. During the longer ramp times (> 1 s) hydrogen, formed by aqueous hydrolysis, diffuses into the plastic zone, resulting in local embrittlement. However, if the test involves a waveform with a hold time component, and a high temperature, the hydrogen diffuses out of the plastic enclave and the crack growth rates are not accelerated from the low to the high category. Short ramp times (~ 1 s) at either temperature do not allow a significant production of hydrogen ions, and the growth rates remain in the low category. The suggested mechanism is supported by fractographic observations of increased intergranular and quasi-cleavage components

for the hydrogen-assisted fatigue-crack growth modes, while the fatigue fracture surfaces of specimens from the low-growth-rate category showed a higher percentage of striation formation and transgranular growth modes.

Sponsor: NRC – NRL Problem No: M01-40

* * * * *

Fractographic and Microstructural Analysis of SCC Specimens of HY-100, HY-130, and HY-180 Steel Weldments

F. W. Fraser and E. A. Metzbower, *Material Science and Technology Division*

Background: The resistance of a welded steel to stress-corrosion cracking (SCC) depends on the microstructure of the weld metal and on fracture separation paths. Variables such as chemical composition, thermal treatment, and welding processes and parameters alter the microstructure, thereby affecting the material's resistance to SCC. An investigation was undertaken to correlate the microstructures, the fracture morphologies, and the SCC resistances of HY-100, HY-130, and HY-180 steel weldments prepared using substantially different welding practices and filler materials.

Progress: A final report on one phase of the problem is being published as NRL Report 8370, "Fractographic and Microstructural Analysis of SCC Specimens of HY-100, HY-130, and HY-180 Steel Weldments," by F. W. Fraser and E. A. Metzbower.

Abstract: This report summarizes an investigation of the microstructures and fracture morphologies of selected double-V weldments of HY-100, HY-130, and HY-180 steels fractured under stress in an aqueous environment. The specimens, which were prepared using substantially different welding practices and filler materials, displayed similar K_{Iscc} values. Optical examination of the microstructures showed that repeated thermal cycling, which occurs during fabrication of GTA (gas-tungsten-arc), fine-bead, as-welded specimens, resulted in a uniform, fine-grained, tempered microstructure that offered the greatest resistance to stress-corrosion cracking (SCC). Microvoid coalescence (MVC) was the dominant fracture mode.

Coarse-bead, as-welded, GMA (gas-metal-arc) specimens contained substantial amounts of high-temperature-transformation products which fractured by cleavage. Heat treating these specimens, to a lower yield strength, refined the microstructure and improved the SCC resistance. The dominant fracture mode of the heat-treated specimens was MVC. Microbranching of the advancing crack front occurred in the coarse-bead, as-welded specimens and may be responsible for the relatively high K_{Iscc} values reported.

Sponsor: DTNSRDC – NRL Problem No: M04-13

* * * * *

Machining Flaws and the Strength-Grain Size Behavior of Ceramics

R. W. Rice, *Material Science and Technology Division*

Background: Single phase as well as some multiphase ceramic polycrystalline bodies, especially those of limited to zero porosity, show a definitive and characteristic dependence of their brittle tensile failure on grain size (G). For most materials, such behavior occurs to temperatures of at least a few hundred degrees centigrade and for many more refractory bodies to temperatures of 1000°C or more. Typically, two regimes of such G dependence of brittle fracture are observed. At larger G, there is typically a significant increase in tensile or flexure strength as G decreases. However, as G decreases below some intermediate level, e.g., below 10 to 50 μm, much less, or possibly no, increase in S is observed with further decreasing G. The latter regime showing more limited or no increase in S with decreasing G typically gives a nonzero intercept on a Petch plot, a plot of S versus $G^{-1/2}$. In the past, such nonzero intercepts have often been interpreted as indicating strength control due to microplastic nucleation or growth of cracks. However, recent fractographic information shows that this is commonly not the case, that flaws, commonly from machining, are typically the source of failure. In the past, it was often assumed that the G dependence of S was due to the flaw size (C) being related to G; i.e., most commonly it was assumed that $C = G$. However,

recent fractographic information shows that the size of flaws introduced by machining does not vary much, if at all, with G. Thus, flaws are typically much smaller than large grains and typically much larger than fine grains. This extensive fractographic information thus invalidates the previous explanation for the grain-size dependence of brittle failure of ceramics under tensile loading. The purpose of this paper is to review the pertinent fractographic observations on machining flaws and S-G data in order to relate the two together and to discuss the mechanisms of failure that they demonstrate or suggest.

Progress: An interim report on the problem has been published as NRL Memorandum Report 4076, "Machining Flaws and the Strength Grain Size Behavior of Ceramics," by R. W. Rice, dated Sept. 29, 1979.

Abstract: A model for the strength-grain size dependence of ceramics failing from machining flaws is presented based on the observation that the size of machining flaws (C) shows little or no dependence on grain size. Two regimes of behavior are seen. At finer grain sizes, little or no strength dependence on grain size (G) exists because flaws are $> G$. For large G, the significant decrease of strength with increasing G is attributed by a transition from polycrystalline to either lower single crystal or grain boundary (i.e., bicrystal) fracture energies as the ~ constant (C) becomes significantly less than the G as G increases. The transition between the two regimes is when C and G are similar. Extensive analysis of strength-grain size data, and more limited directly correlated fractographic data support the proposed model. Spontaneous cracking in noncubic materials is shown to support the model, but not to be an alternate explanation for the transitions seen in machined Al_2O_3 or BeO. This analysis also further supports the observation that machining flaws do not vary greatly with typical variations in machining parameters.

Sponsor: ONR -- NRL Problem Nos: M05-12 and P03-19

* * * * *

The Nature of Strength-Controlling Machining Flaws in Ceramics

R. W. Rice and J. J. Mecholsky, Jr., *Material Science and Technology Division*

Background: Machining of most glasses, single crystals, and dense polycrystalline specimens is typically assumed to introduce flaws which control their mechanical strength. However, in discussing the evidence for such flaw-controlled failure vs dislocation-controlled failure, Rice previously pointed out that there had been little or no direct verification of flaw failure. This paper summarizes and significantly extends recent work on the nature of flaws introduced in a variety of ceramic materials as a function of various machining and specimen parameters. The natures of the two flaw populations that result in the common anisotropy of strength associated with different grinding directions are treated first. Then, more limited studies of other modes of machining are compared with these grinding studies, followed by some discussion of flaw variations and distributions.

Progress: An interim report on the problem has been published as NRL Memorandum Report 4077, "The Nature of Strength Controlling Machining Flaws in Ceramics," by R. W. Rice and J. J. Mecholsky, Jr., dated Sept. 25, 1979. AD-A075 481.

Abstract: The nature of machining flaws introduced in a variety of glass, single-crystal, and especially polycrystal bodies is reported, based on fractographic determination of such flaws as the source of mechanical failure. Particular attention is given to grinding where the anisotropy of strength due to the direction of grinding relative to the tensile axis is shown to be due primarily to a dual population of flaws of differing shapes. One set of flaws forms perpendicular and another parallel to the grinding direction. The latter flaws are typically substantially more elongated and often larger than the former and thus give lower strengths for stressing perpendicular to the direction of grinding. Sawing, sanding, and polishing are also shown to result in similar dual flaw populations. The character of flaws is examined as a function of the type of material and machining, as well as of specimen size and shape. The latter suggests a limited strength-size effect due to machining flaws. However, the key findings are that machining flaws do not vary greatly with typical variations of machining or material parameters, e.g., composition, grain size, or hardness.

Sponsor: ONR NRL Problem Nos: M05-12 and P03-19

OCEAN SCIENCES

Distortion of Internal Wave Patterns by Background Shear: A Case Study

T. H. Bell, Jr., *Ocean Sciences Division*

Background: Sheared background currents are known to exert a profound influence on the structure and evolution of internal wave patterns in density-stratified fluid systems such as the upper ocean. The purpose of this study is to provide some fundamental quantitative information on the distortion of internal wave patterns in a realistic upper-ocean environment. The emphasis is on how certain characteristic features of internal wave patterns observed in the absence of shear are distorted by the presence of background shear.

Progress: An interim report on the problem is being published as NRL Report 8362, "Distortion of Internal Wave Patterns by Background Shear: A Case Study," by T. H. Bell, Jr.

Abstract: This report constitutes a preliminary comparative study of the structure of numerically simulated internal-wave patterns with and without background shear. The analysis focuses on two distinct aspects of the wave pattern: the energy envelope (that region of space within which appreciable density perturbations occur), and the phase information (the structure of the density perturbations within the energy envelope). Using real background oceanographic data, we examine how the energy envelope and phase information observed in the absence of shear are distorted by the presence of background shear. The relevant parameter for determining the relative importance of the background shear is shown to be the bulk, rather than local, Richardson number, defined in terms of characteristic density and velocity variations over the characteristic dimensions of the wave pattern, rather than in terms of local derivatives of the background density and velocity profiles. Because of the influence of the larger-scale, averaged properties of the shear profile on the wave-propagation process, the net drift velocity of the energy envelope at any depth level does not accurately reflect the background current speed at that level. Shear induced restrictions of the vertical extent of the energy envelope are shown to be consistent with elementary wave-propagation arguments relating to the so-called critical-layer phenomenon. Insofar as the phase information is concerned, we find significant coherence losses (relative to unsheared patterns) over several Brunt-Väisälä periods.

Sponsor: NAVMAT NRL Problem No: 1103-0

PLASMA PHYSICS

Cross-Field Jetting of Energetic Ions Produced by Rayleigh-Taylor Instability

S. H. Brecht, *Science Applications, Inc.*
K. Papadopoulos, *Plasma Physics Division*

Background: A high-attitude nuclear explosion (HANE) can lead to cross-field transport of debris, which in turn produces energetic trapped betas on L shells considerably higher than the one on which the detonation took place. The jetting model currently used in the SPECTER code is an estimate from ad hoc arguments. In this work the cross-field transport of charged debris, during expansion of the debris sphere, is modeled by considering the Rayleigh-Taylor instability in a linear calculation. The model considers three phenomena. Two provide energy sources for the instability and the third provides a damping mechanism. The damping mechanism allows estimates of minimum wavelengths for the modes as well as critical thickness and temperatures for onset of the instability.

The first phenomenon which can initiate the Rayleigh-Taylor instability is the laminarlike accelerations of a percentage of the ions within the shock. Essentially, this leads to a three-species description of the plasma. Particle simulations of an advancing shock have demonstrated the existence of these accelerated

ions, which have densities of approximately 10% of the ion density in the shock. The third species causes a space charge with the resultant electric field. The result of this is the Rayleigh-Taylor instability. The second source of energy for the instability is the curvature of the magnetic field lines caused by the bubble expansion. This force is more apparent during early phases of the bubble evolution. Finally, there is damping of the instability provided by finite Larmor radius corrections to the momentum equations (i.e., magnetic viscosity). The damping is a function of the instability wavelength and is directly coupled to the thickness of the debris shell as well as to the perpendicular pressure of the debris.

Progress: An interim report on the problem has been published as NRL Memorandum Report 4068, "Cross Field Jetting of Energetic Ions Produced by Rayleigh-Taylor Instability," by S. H. Brecht and K. Papadopoulos, dated Oct. 3, 1979.

Abstract: The phenomenon of cross-field jetting of debris following a nuclear detonation is explained by the Rayleigh-Taylor instability. The growth rate for the mode is calculated as well as thresholds for onset and wavelength. A model for this phenomenon is developed and the amount of debris transported across the field lines is estimated.

Sponsor: DNA — NRL Problem No: H02-53

* * * * *

Development of Imploding-Liner Systems for the NRL LINUS Program

P. J. Turchi, R. L. Burton, A. L. Cooper, R. D. Ford, D. J. Jenkins, J. Cameron, and R. Lanham
Plasma Physics Division

Background: The earliest work on imploding liner magnetic flux compression is associated with weapons development and the use of explosives to implode metal shells. The compression of trapped magnetic flux was used as a measure of the implosion of the shell, whose position was otherwise difficult to ascertain. Later analysis indicated the possibility of creating ultrahigh magnetic fields by this technique, and efforts were made along these lines by various groups. Some of these efforts were closely associated with the development of explosive flux-compression or magnetocumulative generators for high-energy pulsed electrical-power systems. With implosions driven by high explosive, magnetic fields of tens of megagauss were achieved.

Later efforts utilized electromagnetic forces, in the manner of z- or theta-pinch discharges, to implode cylindrical liners and achieved peak fields of a few megagauss. In principle then, imploding-liner magnetic flux compression techniques could thus be coupled to pulsed electrical-power sources, allowing repetitive operation of ultrahigh magnetic field plasma compression systems. (Indeed, attempts had already been made to compress plasma using imploding liners, driven by explosives; these tests indicated that considerable development, involving many explosive shots and improved initial plasma systems, would be required to achieve success.)

The concept of using magnetic-flux compression to create and confine a high-temperature, high-density fusion plasma had been suggested and discussed by several authors. It had, however, fallen into disfavor, in part because of the success of other techniques (e.g., theta pinches driven by fast capacitor banks) but, more importantly, because of the difficulty of conceiving and demonstrating liner-implosion flux compression techniques that could extrapolate to controlled repetitive situations required for fusion-power reactors. Some new enthusiasm, however, developed at IAE Kurchatov, based on electromagnetic liner implosion and MHD conversion of liner material energy after neutron-induced vaporization subsequent to thermonuclear burn. After discussions between E. P. Velikhov, of IAE Kurchatov, and R. A. Shanny, of NRL, theoretical and numerical calculations of imploding liner fusion techniques were performed at NRL within a program called *LINUS*. Initial experiments with metal liners imploded in the manner of a theta pinch using a 50-kJ capacitor bank (SUZY I) were performed at NRL by D. C. dePackh, J. Okada, M. P. Young, and others. (These experiments included some tests with lithium liners that were quite spectacular, since the hot lithium fragments would break out of the sealed container after implosion and react with the

surrounding air.) Development of higher-energy systems was initiated by dePackh et al, including work on a homopolar generator with liquid-metal brushes, superconducting inductive-opening switches, and a new fast capacitor bank (SUZY II) to provide liner implosions at the 500-kJ level. After the retirement of dePackh in 1972, the work on homopolar generators and inductive-opening switches was continued by A. E. Robson, P. J. Turchi, and others. With the completion of the SUZY II capacitor bank, the electromagnetic implosion of solid cylindrical shells was continued by Turchi, aimed at the demonstration of large radius-ratio implosions (20 to 30:1) of adequate symmetry and quality to achieve megagauss magnetic fields. In parallel with the experimental efforts, theoretical and numerical studies were continued by J. P. Boris and N. K. Winsor on modeling liner implosions, and by A. Barcilon, D. L. Book, A. L. Cooper and Winsor on the rotationsl stabilization of Rayleigh-Taylor modes in liquid liner implosions, following the suggestion of Shanny. The initial scheme for liner-plasma compression was a simple long cylindrical liner and plasma, following work at IAE Kurchatov. Later, Robson proposed the use of two imploded, opposing rings to compress a spindle cusp plasma (the "flying cusp") and Turchi suggested a cusp-ended theta pinch to restore basically cylindrical liner motion and allow a reversible liner-plasma compression cycle.

Progress: An interim report on the problem has been published as NRL Memorandum Report 4092, "Development of Imploding Liner Systems for the NRL LINUS Program," by P. J. Turchi, R. L. Burton, A. L. Cooper, R. D. Ford, D. J. Jenkins, J. Cameron, and R. Lanham, dated Sept. 28, 1979, AD-075 005.

Abstract: For nearly two decades, the idea of creating fusion plasmas by the implosion of cylindrical *shells* or liners has appealed to workers interested in high-energy-density systems. A variety of schemes have been offered over the years to accomplish the adiabatic compression of plasmas at megagauss magnetic-field levels by imploding-liner magnetic-flux-compression techniques. The two main elements of such schemes have been the implosion of an electrically conducting cylindrical liner and the creation of an initial plasma suitable for compression by the surrounding liner. Some progress has been made both experimentally and conceptually in regard to plasmas that could be compressed by liner implosion, but no experimental test has yet been accomplished successfully in which the energy and temperature of the magnetically confined plasma has been increased into a significant regime by liner implosion. Considerable progress has been made, however, in developing liner implosion techniques suitable for both experimental development and eventual imploding-liner fusion reactors. The principal development has been the achievement of controlled, reversible liner implosions with excellent symmetry and surface quality. This paper reviews some of the highlights of the development of liner implosion systems at the Naval Research Laboratory and indicates directions of future work.

Sponsors: ONR and DoE NRL Problem Nos: H02-28D and H02-26E

* * * * *

Electromagnetic Instabilities in a Focused Ion Beam Propagating Through a z-Discharge Plasma

P. F. Ottinger, D. Mosher, and S. A. Goldstein, *Plasma Physics Division*

Background: In an earlier paper, it was shown that focused ion beams for use in a pellet fusion device can propagate axially down a z-discharge plasma channel without generating disruptive microturbulence due to electrostatic streaming instabilities. The azimuthal magnetic field in the z-discharge channel confines the beam radially as it propagates. Here the analysis is extended to study electromagnetic velocity-space instabilities. In particular, the Weibel instability ($\mathbf{k} \cdot \mathbf{B} = 0, \mathbf{k} \quad \mathbf{V}_z \approx 0$) and the Whistler instability ($\mathbf{k} \times \mathbf{B} \approx 0, \mathbf{k} \cdot \mathbf{V}_z \approx 0$) are investigated, where $\mathbf{k}$ is the wave vector, $\mathbf{B}$ is the azimuthal magnetic field, and $\mathbf{V}_z = V_z \hat{e}_z$ is the axial streaming velocity of the beam.

The beam-plasma system consists of a focused ion beam (typically a 5-MeV proton beam of 50-ns duration, 0.5-cm radius, and a current of 5×10^5 A) propagating down the axis of a z-discharge plasma channel. The ion beam is focused at the entrance to the plasma channel with velocity components transverse to z given by $V_\perp / V_z \approx \tan \theta << 1$. A high plasma density in the channel ($n_p \approx 10^{18}$ cm^{-3}) insures

good beam-charge neutralization. Good beam-current neutralization in the interior of the beam also occurs, so that the total magnetic field is comparable to that associated with the preformed channel established before beam injection. The beam current greatly exceeds that establishing the channel, so the electron drift velocity is approximated by $V_e \approx n_b V_z / n_p$.

Hydrodynamic modeling of the background plasma shows that a uniform channel net-current model is appropriate for the early times associated with passage of the beam front. This is because the low-temperature channel is established microseconds before beam injection, so that complete magnetic diffusion occurs. Later in the ion pulse, expansion of the beam-heated high-temperature plasma ($T \approx 25$ to 50 eV) reduces the magnetic field strength in the interior of the channel. The built-up field in the expanding cylindrical shock wave is also enhanced by significant current nonneutralization in the cool plasma surrounding the beam-heated channel. The maximum field strength just outside the ion-beam radius can exceed that established by the initial z-discharge current by a large factor. Thus, at late times during beam passage, the magnetic-field distribution is closely approximated by a surface-current model.

Progress: An interim report on the problem has been published as NRL Memorandum Report 4088, "Electromagnetic Instabilities in a Focused Ion Beam Propagating Through a z-Discharge Plasma," by P. F. Ottinger, D. Mosher, and S. A. Goldstein, dated Oct. 15, 1979.

Abstract: A beam-plasma system consisting of a focused light ion beam propagating through a z-discharge plasma is analyzed for electromagnetic velocity space instabilities. In particular, the Weibel ($\mathbf{k} \cdot \mathbf{B} = 0$, $\mathbf{k} \cdot \mathbf{V}_z \approx 0$) and the Whistler ($\mathbf{k} \times \mathbf{B} \approx 0$, $\mathbf{k} \cdot \mathbf{V}_z = 0$) instabilities are studied. It is found that unstable modes do not grow fast enough to affect the beam propagation in a pellet-fusion-reactor chamber. For $\mathbf{k} \cdot \mathbf{V}_z \gtrsim 0$, the instabilities convect with a velocity much less than the beam streaming velocity.

Sponsor: DoE NRL Problem No: H02-29B

* * * * *

The Nonlinear Theory of Free-Electron Lasers and Efficiency Enhancement

P. Sprangle and W. M. Manheimer, *Plasma Physics Division*
C. M. Tang, *Jaycor*

Background: Free-electron lasers (FELs) based on backscattering from relativistic electron beams have demonstrated a unique potential for becoming a new type of coherent radiation source. In principle, these radiation sources will be characterized by output wavelengths ranging from the millimeter to beyond the optical regime, frequency tunability, very high power levels and high efficiencies. Theoretical analysis on the FEL mechanism has been carried out in the single-particle as well as the collective-scattering regime. Also, nonlinear processes and saturation efficiencies have been considered for various FEL scattering regimes.

The operative mechanism in FELs is a parametric process in which a long-wavelength pump field interacts with a beam of relativistic electrons. Under certain conditions the incident pump field will decay into a longitudinal wave (density wave) and a backscattered electromagnetic wave which is double Doppler upshifted in frequency. The longitudinal wave (also referred to as density wave, beat wave, or ponderomotive wave) results from the coupling of the pump field and the electromagnetic field through the $\mathbf{v} \times \mathbf{B}/c$ force term. The ponderomotive wave plays a central role in the linear and nonlinear development of the scattering process. Its effect on the electron beam is closely analogous to the role played by the negative energy (slow space charge) wave in conventional traveling-wave mechanisms.

The pump field may take the form of a static, spatially periodic magnetic or electric field or a propagating electromagnetic wave. In this work we take the pump to be a static, periodic right-handed, helically polarized magnetic field. The frequency of the scattered radiation is given by

$$\omega \approx (1 + v_z/c)\, \gamma_z^2\, v_z\, (2\pi/l) \approx 4\pi \gamma_z^2\, c/l,$$

where

$$\gamma_z = (1 - v_z^2/c^2)^{-1/2},$$

v_z is the axial beam velocity, c is the speed of light, and l is the pump period. The possibility of using a two-stage FEL scattering process to reduce the electron energy required for very short output wavelengths has been suggested.

Roughly speaking, FELs can be divided into two categories, depending on the gain of the radiation field. In the low-gain regime, the overall spatially integrated gain is due to wave interference effects and is much less than unity. This is a single-particle scattering regime (collective effects are not manifested through space-charge fields) and is exemplified by experiments at Stanford University. The high-gain FELs are characterized by stimulated radiation fields which grow exponentially in the linear regime. Experiments with intense relativistic electron beams performed at NRL, Columbia University, and Cornell University fall into this class. A detailed theoretical discussion of the various FEL mechanisms can be found in Refs. 1-3.

The main objectives of this work are to present a self-consistent nonlinear formulation of the FEL mechanism and to analyze theoretically some of the concepts necessary to develop efficient, high-power, tunable FEL radiation sources. Some of the salient features of this theory include completely arbitrary magnetic-pump field (period and amplitude can be functions of axial position), space-charge effects, arbitrary polarization of the radiation field, completely relativistic particle dynamics, and frequency and spatial harmonics in the excited fields. The nonlinear formalism developed for the FEL problem is also applicable to a large class of temporal-steady-state convective processes. Our formulation of the problem permits the spatial dependence of the pump magnetic field to be arbitrary. Hence, efficiency-enhancement schemes which utilize amplitude and wavelength spatial variations of the pump field can be analyzed. The spatial variation of the scattered radiation amplitude and wavelength occurs on a scale length which is large compared to the wavelength of the pump field. This permits numerical solutions for cases where the electron-beam energy is extremely high. That is, in this approach there is no large separation of spatial scale lengths, despite the large spatial scale difference between the wavelength of the scattered field and the pump field, so arbitrarily high values of the relativistic gamma factor associated with the beam can be considered. Furthermore, the formulation is carried out in the laboratory frame under temporal-steady-state conditions.

Progress: An interim report on the problem has been published as NRL Memorandum Report 4034, "The Nonlinear Theory of Free Electron Lasers and Efficiency Enhancement," by P. Sprangle, C. -M. Tang, and W. M. Manheimer, dated Sept. 28, 1979. AD-A075 063.

Abstract: The development of lasers in which the active medium is a relativistic stream of free electrons has recently evoked much interest. The potential advantages of such free-electron lasers include, among other things, continuous frequency tunability, very high power of operations and high efficiency. The free electron laser is characterized by a pump field, for example, a spatially periodic magnetic field, which scatters from a relativistic electron beam. The scattered radiation has a wavelength much smaller than the pump wavelength, depending on the electron beam energy. We present a general self-consistent nonlinear theory of the free-electron laser process. The nonlinear formulation of the temporal-steady-state free-electron laser problem results in a set of coupled differential equations governing the spatial evolution of the amplitudes and wavelength of the radiation and space-charge fields. These equations are readily solved numerically, since the amplitude and wavelength vary on a spatial scale comparable to a growth length of the output radiation. A number of numerical/analytical illustrations are presented ranging from the optical to the submillimeter wavelength regime. Our nonlinear formulation in the linear regime is compared with linear theory and agreement is found to be excellent. Analytical expressions for the saturated efficiency and radiation amplitude are also shown to be in very good agreement with our nonlinear numerical solutions. Efficiency curves are obtained for both the optical and submillimeter FEL examples with fixed magnetic-pump parameters. We show that these intrinsic efficiencies can be greatly enhanced by appropriate contouring of the magnetic-pump period. In the case of the optical FEL, the theoretical single-

pass efficiency can be made greater than 20% by appropriate decrease of the pump period and increase of the pump magnetic field.

REFERENCES

1. N. M. Kroll and W. A. McMullin, *Phys. Rev. A* 17:300 (1978).
2. P. Sprangle, R. A. Smith, and V. L. Granatstein, "Free Electron Lasers and Stimulated Scattering from Relativistic Electron Beams," NRL Memorandum Report 3911, Dec. 8, 1978, AD-A066 177 (*Rept. NRL Prog.*, Jan. 1979, pp. 22-23).
3. P. Sprangle and R. A. Smith, "The Theory of Free Electron Lasers," NRL Memorandum Report 4033, Sept. 18, 1979, AD-A075 363 (*Rept. NRL Prog.*, Oct. 1979).

Sponsors: DARPA and ONR – NRL Problem Nos: R18-16B and R08-59

* * * * *

A Theory of Anomalous Absorption, Backscatter, and Flux Limitation in Laser-Produced Plasmas

D. G. Colombant and W. M. Manheimer, *Plasma Physics Division*

Background: The absorption and backscatter of light in the underdense blowoff of a laser-produced plasma and a limitation of electron thermal-energy flux play important roles in laser fusion. This work constitutes a one-dimensional fluid simulation of these and other relevant processes. It is a continuation of our earlier work in this area, but it models the dynamics of the interaction rather than the steady state. Also included in this work is a study of the effects of Brillouin backscatter. Although our work applies in principle to any laser-produced plasma, it is particularly motivated by experiments at the Naval Research Laboratory. Experiments there have demonstrated that backscatter through the lens (apparently Brillouin backscatter) can be a very important process for structured laser pulses at sufficiently high intensity. Also, more recent experiments with longer pulses (pulse duration of about 3 ns) have shown very high absorption even at intensities where inverse bremsstrahlung is not effective. For instance, at an irradiance of 7×10^{14} W/cm^2 the fractional absorption is about 60%. Also, experiments at NRL and elsewhere have shown that absorption is enhanced when the target is in the focal plane of the lens. It has always been our opinion that resonant absorption alone cannot account for all of the absorption. Absorption measurements done at many laboratories lead to this conclusion. The additional mechanism we propose is ion acoustic turbulence driven by the return current. That mechanism takes place in either an unmagnetized or a magnetized plasma. The fluid simulations reported here attempt to model this process. A very much oversimplified picture is that ion acoustic turbulence in the underdense plasma begins to take over where classical inverse breamsstrahlung becomes ineffective. Roughly speaking, ion acoustic turbulence at high temperature gives perhaps half as much absorption as inverse bremsstrahlung at low temperature.

Progress: An interim report on the problem has been published as NRL Memorandum Report 4083, "A Theory of Anomalous Absorption, Backscatter, and Flux Limitation in Laser-Produced Plasmas," by D. G. Colombant and W. M. Manheimer, dated Oct. 11, 1979. AD-A075 350.

Abstract: Fluid simulations of laser light absorption and backscatter are presented for various laser irradiances, wavelengths, target materials, laser pulse lengths, and simulated prepulse conditions. Physical processes included in the model are inverse bremsstrahlung, resonant absorption, absorption by ion-acoustic fluctuations, and Brillouin backscatter. For the anomalous processes, self-consistent transport coefficients are derived and used throughout the time-dependent, one-dimensional code. Flux limitation is thus taken into account as a result of the physical processes included. Interplay between the various absorption mechanisms and backscatter are uncovered in this study. Comparisons with experiments are presented and suggestions for further experiments are made.

Sponsor: DoE NRL Problem No: H02-58A

PAPERS BY NRL STAFF MEMBERS

FORMAL REPORTS

8320 **"Passive Infrared Surveillance, Part I: Model Formulation,"** by R. A. Steinberg, dated Sept. 28, 1979. Interim Report on NRL Problem N01-29. (EOTPO Report No. 52). AD-A075 603.

8327 **"The NRL-EPRI Research Program (RP886-2), Evaluation and Prediction of Neutron Embrittlement in Reactor Pressure Vessel Materials, Annual Progress Report for CY 1978,"** edited by J. R. Hawthorne, dated Aug. 30, 1979. Progress report on NRL Problem M01-60. AD-A075 012.

8329 **"Design Manual for a Constant Beamwidth Transducer,"** by A. L. Van Buren, dated Oct. 11, 1979. Interim report on NRL Problem S02-50. AD-E000 330.

8334 **"Broadband GaAs MESFET Power Amplifier Design Aspects,"** by H. A. Willing and W. H. Ku, dated Oct. 12, 1979. Final report on one phase of NRL Problem R08-87. AD-A075 692.

PAPERS APPEARING IN RECENT ISSUES OF SCIENTIFIC JOURNALS

ACOUSTICS

1. **"Compact Parametric Hydrophone Using Nonlinear Interaction Within a Cylindrical Rubber Waveguide,"** by R. D. Corsaro and J. Jarzynski, *J. Acoust. Soc. Am.* **66**(3):895-904, Sept. 1979.

This paper investigates the effects of placing a rubber cylinder between the pump and receiving transducers in an otherwise conventional parametric receiver. The use of this rubber cylinder is experimentally found to increase parametric conversion gain by 20 to 24 dB, while simultaneously reducing beam width by a factor of two to three. These improvements are relative to the same pump-receiver separation distance (0.23 m) in water alone, over the experimental frequency range of 4.8 to 23 kHz. A theoretical model of this configuration is developed, using the numerical solution of the system of equations obtained by coupling the interior surface Helmholtz equation to the integral equation for the exterior of the cylinder. The resulting calculated beam patterns and efficiency levels are found to be in very good agreement with the data collected. Using this model, the observed efficiency improvement is found to be largely due to the slow speed of sound in this rubber (1018 m/s) as compared to water, while the directivity improvement is, to a significant extent, due to the acoustic slow-waveguide effect.

2. **"Derivation of the Acoustic Wave Equation in the Presence of Gravitational and Rotational Effects,"** by J. A. DeSanto, *J. Acoust. Soc. Am.* **66**(3):827-830, Sept. 1979.

We derive, from first principles, the multidimensional partial differential equation obeyed by the underwater pressure field in the presence of gravitational and rotational forces acting on the fluid medium. The result is valid for a sound speed which depends on all three spatial dimensions and time. For the special case of a purely depth-dependent sound speed the result reduces essentially to that of Tolstoy. The relationship to the internal wave equation is also presented, as well as other examples, including the effect of Rossby waves.

3. **"Mesoscale Variations in the Deep Sound Channel and Effects on Low-Frequency and Propagation,"** by W. J. Emery, T. J. Reid, J. A. DeSanto, R. N. Baer, and J. P. Dugan, *J. Acoust. Soc. Am.* **66**(3):831-841, Sept. 1979.

Spatial variability in the deep sound channel is measured in a large-scale oceanographic survey, and its effects on sound propagation are studied in a numerical experiment. The oceanographic data are obtained from a near-synoptic, multiship survey of upper layer thermal structure in the Northwest Pacific which is extended to 4000-m depth using an objective extrapolation model and historical hydrographic data. The extrapolated temperature profiles are converted to salinity and sound-velocity profiles using mean temperature-salinity curves, and the resultant sound-velocity structure is dominated by mesoscale features which are apparent as large, vertical excursions of the channel depth. A numerical experiment that models low-frequency (50-Hz) sound propagation in this model ocean shows that the standard deviation of an ensemble intensity field rises to a plateau of about 5.5 dB in several tens of kilometers, indicating a mesoscale multipath effect with a shorter saturation range than the corresponding internal-wave-induced effect. Statistics of the intensity at a point receiver are shown to be slightly non-Gaussian, with the nonnormal deviation decreasing with depth.

4. **"The Ocean Crust West and North of the Svalbard Archipelago: Synthesis and Review of New Results,"** by P. R. Vogt, R. H. Feden, O. Eldholm, and E. Sundvor, *Polarforschung* **48**(1/2):1-19 (1978).

A large amount of new geophysical data have been collected in the deepwater areas around the Svalbard archipelago in the last half-decade. Within the area of permanent ice cover these data are primarily detailed aeromagnetic surveys, supplemented by a few bathymetric profiles collected by submarines. Areas open to surface ships have been investigated using 3.5 Kc bathymetry, single and multi-channel reflection profiling, sonobuoy and two-ship refraction, gravity, magnetic, heat flow, and other techniques. This paper summarizes these new geophysical data for the benefit of earth scientists investigating the Svalbard area. The seafloor-spreading phase of the plate-tectonic evolution of the Greenland-Norwegian Sea and Eurasia Basin began 57 to 58 m.y.b.p. during the reversed interval prior to anomaly 24. Svalbard and northeast Greenland slid past each other until about 36 m.y.b.p., when Greenland became attached to the North American plate. Subsequently, spreading from the Knipovich Ridge has been complex, including oblique spreading and probable eastward jumps of the accretion axis. The "Yermak" hot spot has been postulated north of Svalbard to explain the Yermak and Morris Jesup Rise plateaus, Cenozoic volcanism in northeast Greenland and on Vestspitsbergen, and other effects.

5. **"A Path-Integral Approach to the Parabolic Approximation. I,"** by D. R. Palmer, *J. Acoust. Soc. Am.* **66**(3):862-871, Sept. 1979.

We use Feynman's theory of path integrals to study the parabolic approximation. With the aid of path-integral representations for the solutions to the parabolic equation and the Helmholtz equation, we show the parabolic approximation, for either the two-dimensional or the three-dimensional parabolic equation, may be decomposed into two simpler approximations: a type of geometric optics or eikonal approximation and a stationary-phase approximation. We then relax the geometric optics approximation by assuming, instead, a variant of the Rytov approximation. This development leads to a two-dimensional parabolic equation which models a three-dimensional ocean. Finally, we discuss the validity of the stationary-phase approximation.

CHEMISTRY

6. **"ArF Laser Photodissociation of NH_3 at 193 nm: Internal Energy Distributions in NH_2 $\tilde{X}^2B_1$ and $\tilde{A}^2A_1$, and Two-Photon Generation of NH $A^3\Pi$ and $b^1\Sigma^+$,"** by V. M. Donnelly, A. P. Baronavski, and J. R. McDonald, *Chem. Phys.* **43**:271-281 (1979).

Ammonia is photolyzed with an ArF excimer laser at 193 nm. NH_2 is formed in the $\tilde{A}^2A_1$ state, detected through the identification of $\tilde{A}^2A_1 \rightarrow \tilde{X}^2B_1$ emission bands between 620 and 1100

nm, and also in the $\widetilde{X}^2B_1$ state, identified by dye laser induced fluorescence on the $\widetilde{A} \leftarrow \widetilde{X}$ transition. The $\widetilde{A}$-state yield is about 2.5% relative to the $\widetilde{X}$-state. The $\widetilde{A}^2A_1$ state has a propensity for being formed in high K_a' rotational levels. ν_2' vibrational levels of the $\widetilde{A}^2A_1$ state appear to be populated in a monotonically decreasing distribution, with an average vibrational energy content of 1000 cm^{-1}. Rotational populations are deduced for the 050 Σ vibrational level of the $\widetilde{A}^2A_1$ state. The colder-than-room-temperature rotational distribution (T_{rot} = 210 ± 40 K) is explained by angular momentum conservation arguments. The vibrational and rotational features observed in the dye laser induced fluorescence excitation spectrum of NH_2 $\widetilde{A} \leftarrow \widetilde{X}$ could not be assigned at near collision-free pressures. However, under thermalized conditions, the 090 ← 000 Σ, 090 ← 000 Δ, 0 100–000 π, and 0 100 ← 000 Φ bands are clearly identified. Arguments are presented which show that the nascent $\widetilde{X}^2B_1$ photo-fragment is created either with the ν_2'' vibrational population or the K_a'' rotational population inverted. NH $A^3\Pi \rightarrow X^3\Sigma^-$ and $b^1\Sigma^+ \rightarrow X^3\Sigma^-$ emission are also detected at 336 and 471 nm, respectively. Formation of NH $A^3\Pi$ and $b^1\Sigma^+$ is attributed to two-photon resonance processes.

7. **"Carbon-13 and Proton Nuclear Magnetic Resonance Spectroscopy of Thermosetting Polymers; Analysis of Tetraglycidyl Methylenedianiline/Diaminodiphenylsulfone Formulations,"** by C. F. Poranski, Jr. and W. B. Moniz, in *Composite Materials: Testing and Design (Fifth Conference), ASTM STP 674*, S. W. Tsai, editor, American Society for Testing and Materials, 1979, pp. 553-565.

The proton nuclear magnetic resonance (NMR) spectrum of a tetraglycidyl methylenedianiline/diaminodiphenylsulfone (TGMDA/DDS) mixture contains regions suitable for the quantitative determination of the resin-to-curing-agent ratio. This ratio, expressed in parts curing agent per hundred parts resin (phr), may be found from a simple expression relating the areas of the two aromatic proton signal regions. Preliminary results obtained on replicate samples of five known formulations were satisfactory with respect to reproducibility, but showed a −2 phr systematic error at curing agents contents above 30 phr. The method is undergoing refinement. The carbon-13 NMR spectrum of these formulations is also suitable for quantitative analysis, but a procedure has not yet been developed.

8. **"Excited State Dynamics and Bimolecular Quenching Processes for $NH_2(\widetilde{A}^2A_1)$,"** by V. M. Donnelly, A. P. Baronavski, and J. R. McDonald, *Chem. Phys.* **43**:283-293 (1979).

Radiative lifetimes and quenching rate constants have been measured for the $\widetilde{A}^2A_1$ state of NH_2, formed through ArF excimer laser photolysis of NH_3 at 193 nm. The $NH_2(\widetilde{A}^2A_1 \rightarrow \widetilde{X}^2B_1)$ emission is discrete, allowing single vibrational and rotational levels to be isolated. An average radiative lifetime of 31 ± 4 μs and an NH_3 quenching rate constant of (6.1 ± 0.2) × 10^{-10} cm^3 $molecule^{-1}$ s^{-1} is found to be independent of the K_a' rotational level and ν_2' vibrational level for K_a' = 1, 4, 5, and 6 and ν_2' = 6, 7, and 8. The 050 Σ level (K_a' = 0) lifetime is slightly longer (46 ± 6 μs) and its quenching rate constant somewhat lower [(5.0 ± 0.2) × 10^{-10} cm^3 $molecule^{-1}$ s^{-1}]. These lifetimes are interpreted as radiative lifetimes of levels of the $\widetilde{A}^2A_1$ state, unperturbed by Renner-Teller coupling with the ground state. The quenching by NH_3 is shown to be predominately electronic quenching of the $\widetilde{A}^2A_1$ state, with vibrational and rotational relaxation within the excited state being at least ten times slower. A second, previously unobserved, long-lived component is found in the decay of broad-band emission, comprising about 15% of the fluorescence intensity between 620 and 890 nm. Its lifetime is ⩾ 100 μs, with an apparent quenching rate constant of 7 × 10^{-11} cm^3 $molecule^{-1}$ s^{-1}. This long-lived emission is ascribed to spare coupling between some levels of the $\widetilde{A}^2A_1$ and $\widetilde{X}^2B_1$ states.

9. **"Formation and Chemiluminescent Decomposition of Dioxetanes in the Gas Phase,"** by D. J. Bogan, J. L. Durant, Jr., R. S. Sheinson, and F. W. Williams, *Photochem. Photobiol.* **30**:3-15 (1979).

High-resolution chemiluminescence spectra have been obtained of the singlet electronically excited products of $O_2(^1\Delta)$ plus alkene, dioxetane forming, reactions. The experiments were conducted in a flow apparatus at pressures of 1 to 5 torr. The spectra are a measure of the unrelaxed

initial distribution of energy in the excited product. Results are reported for ethylene, 1,1-difluoroethylene, methyl vinyl ether, ethyl vinyl ether, *n*-butyl vinyl ether, ketene, ketene-d_2, allene, *unsym*-dimethyl allene, dimethyl ketene, 2-methoxy propene, 1-ethoxy propene, 2-bromo propene, and *N,N*-dimethyl isobutenyl amine. Chemiluminescence activation energies, representing the cycloaddition process, and absolute quantum yields for singlet excited product, ranging from 10^{-4} to 2.5×10^{-2}, are reported for 10 alkenes. Several of the reactions, 1,1-difluoroethylene, ketene, ethylene, and allene give formaldehyde $^1n\pi^*$ product with excess vibrational-rotational energy and a higher quantum yield than reactions not displaying this phenomenon. This is an indication of at least partially statistical partitioning of the energy in excess of that needed to electronically excite the formaldehyde. The experiments with ketene and ketene-d_2 provide the first evidence for the existence of unsubstituted 1,2-dioxetanone. The results from several of the experiments, particularly those with 2-methoxy propene and 1-ethoxy propene, are consistent with the mechanism of Goddard, which predicts regioselective and stereoselective attack of $O_2(^1\Delta)$ upon alkoxy substituted alkenes having allylic hydrogen.

10. **"Reactions of $C_2(X^1\Sigma_g^+)$ Produced by Multiphoton UV Excimer Laser Photolysis,"** by L. Pasternack and J. R. McDonald, *Chem. Phys.* **43**:173-182 (1979).

$C_2(X^1\Sigma_g^+)$ disappearance rate constants at 298 K have been determined for reactions with H_2: $(1.38 \pm 0.06) \times 10^{-12}$ cm^3 s^{-1} molecule^{-1}; CH_4: $(1.87 \pm 0.05) \times 10^{-11}$ cm^3 s^{-1} molecule^{-1}; C_2H_6: $(1.59 \pm 0.05) \times 10^{-10}$ cm^3 s^{-1} molecule^{-1}; C_2H_4: $(3.26 \pm 0.05) \times 10^{-10}$ cm^3 s^{-1} molecule^{-1}; C_2F_4: $(5.99 \pm 0.14) \times 10^{-11}$ cm^3 s^{-1} molecule^{-1}; O_2: $(2.82 \pm 0.09) \times 10^{-12}$ cm^3 s^{-1} molecule^{-1}; and CO_2: no apparent reaction. The $C_2(X^1\Sigma_g^+)$ was produced by multiphoton UV excimer laser photodissociation of hexafluorobutyne-2. These results are compared to the reaction rates of $C_2(a^3\Pi_u)$. The rates for O_2 reactions are the same for both C_2 states and no reaction is observed for CO_2 with either C_2 state. However, $C_2(X^1\Sigma_g^+)$ reacts considerable faster than $C_2(a^3\Pi_u)$ with hydrogen and hydrocarbons. The presence of an allowed hydrogen atom exchange reaction for ground state C_2 to form ground state C_2H which is forbidden for metastable triplet C_2 is postulated to account for the disparities in reaction rates. Electronic orbital correlation effects are proposed as an explanation.

11. **"Solution Photochemistry and Kinetics of Palladium(II) Complexes,"** by J. C. Cooper, D. L. Venezky, and T. Lorenz, in *Fundamental Research in Homogeneous Catalysts*, Vol. 3, edited by Minoru Tsutsui, Plenum, New York, 1979, pp. 847-857.

Recent work with palladium(II) complexes as homogeneous catalysts for oxidation of olefins, conversion of carbon dioxide and hydrogen to formic acid, and studies of carbonate-palladium(II) complexes, and involvement of such complexes in some catalytic systems, led us to investigate the equilibria leading to creation of a catalytic site in aqueous solution. Such studies provide insight into the nature of homogeneous catalysis, and related photochemical investigations of palladium complexes suggest possible new catalytic reactions and enhancement of known reactions.

COMMUNICATIONS SCIENCES

12. **"Experiments with Some Algorithms that Find Central Solutions for Pattern Classification,"** by J. Slagle, *Commun. ACM* **22**(3):178-183, Mar. 1979.

In two-class pattern recognition, it is a standard technique to have an algorithm finding hyperplanes which separates the two classes in a linearly separable training set. The traditional methods find a hyperplane which separates all points in one class from all points in the other, but such a hyperplane is not necessarily centered in the empty space between the two classes. Since a central hyperplane does not favor one class or the other, it should have a lower error rate in classifying new

points and is therefore better than a noncentral hyperplane. Six algorithms for finding central hyperplanes are tested on three data sets. Although frequently used in practice, the modified relaxation algorithm is very poor. Three algorithms which are defined in the paper are found to be quite good.

13. **"Flow-Form Implementation of a Linear Predictive Coder for Speech Communication,"** by G. S. Kang, L. J. Fransen, and E. L. Kline, in *Real-Time Signal Processing II*, **SPIE 180**:15-24 (1979).

A number of real-time linear predictive coders (LPCs) have been developed to compress speech waveforms to 2400 bits per second (bps). Most of these LPCs employ a central processing unit (CPU) to analyze a stream of speech samples on a frame-by-frame (block-form) basis. While physical size, weight, and power dissipation of these units have been decreasing steadily, the operation of a battery-powered hand-carried unit is far from realization. This paper presents the flow-form implementation of an LPC as an alternative to the block-form CPU intensive approach. The flow-form implementation of an LPC allows for decentralized, semiautonomous, arithmetic-intensive segments which are supplemented by a microprocessor. The microprocessor performs relatively nontaxing logic operations and computations. Flow-form analysis computation is highly systematic and repetitive, making this form of analysis well suited for very large scale integration (VLSI). Because flow-form analysis does not require a large array of stored data, less data memory is required and power dissipation is reduced. With current technology an LPC can be implemented using fewer than ten chips and having a total power dissipation of less than three watts. The flow-form LPC is comparable in performance to the block-form LPC, and the two units are interoperable, provided the same coding rules and data transmission formats are used.

ELECTRONICS TECHNOLOGY

14. **"Contact-Free Conductivity of Layered Materials: Na β-Alumina,"** by U. Strom and P. C. Taylor, *J. Appl. Phys.* **50**(9):5761-5763, Sept. 1979.

The ionic conductivity and its thermal activation energy have been measured in Na β-alumina using a contact-free induced-torque method at frequencies between 1 and 20 Hz and temperatures between 295 and 415 K. The results are in good agreement with the most recent dc contact conductivity measurements.

15. **"Optical Characterization of Semiconductors,"** by E. D. Palik and R. T. Holm, in *Nondestructive Evaluation of Semiconductor Materials and Devices*, edited by Jay N. Zemel, Plenum, New York, 1979, pp. 315-395.

A review is made of numerous optical techniques for determining parameters such as free-carrier density, mobility, film thickness, and nonstoichiometry. The spectral range of interest varies from the visible to the mm-microwave region, depending on the phenomenon measured. Such topics as thin films on substrates, internal reflection, infrared plasma reflection, cyclotron resonance, ion-implanted layers, laser scanning, band-gap variation in alloys, electroreflectance, and photoluminescence are discussed.

ENVIRONMENTAL SCIENCES

16. **"The Effects of Clouds on the Diurnal Variation of Underwater Irradiances on Horizontal Surfaces,"** by J. A. C. Kaiser, *J. Phys. Oceanogr.* **9**(5):1036-1041, Sept. 1979.

Measurements of underwater downwelling D, underwater upwelling U, both at 5 m, and surface downwelling irradiance I were taken over most of a 5-day period in August and September 1974 south and west of Bermuda. On clear days D/I reached a pronounced maximum at local noon, whereas U/I had a weak minimum at midday. On cloudy days both of the above ratios were larger at all

times of the day and did not exhibit the midday maximum. An absorption model for D/I is constructed by decomposing I into components from the sun, clear sky, and clouds. The major differences between the components is their spectral and radiance distributions. Atmospheric water vapor and sea surface roughness effects are included. The model agrees with the experimental values of D/I to within 5% of I for all the data, and it reproduces the variation of this ratio with solar zenith angle and cloud cover.

17. **"Lagrangian Wind and Current Vectors Very Close to a Short-Fetch Wind-Swept Surface,"** by A. H. Schooley, *J. Phys. Oceanogr.* **9**(5):1060-1063, Sept. 1979.

Drag used in aeronautics and wind stress used in oceanography are essentially equivalent under short-fetch conditions, where the wind velocity substantially exceeds the water velocity. Likewise, lift and wave height are related under the same conditions. An average short-fetch wind velocity of 10 m s^{-1} shows the properties of increasing drag and lift from the trough to the skewed downwind peak. Immediately after the peak the drag and lift drop to a low value corresponding to a region of aerodynamic stall. Recovery is rapid and the process is repeated for the next wave. In spite of the similarities, short-fetch water waves are not well designed air foils. They are somewhat like flying an airfoil backward.

18. **"Silicones as Tracers for Anthropogenic Additions to Sediments,"** by R. Pellenbarg, *Marine Pollution Bull.* **10**(9):267-269, Sept. 1979.

Polyorganosiloxanes (silicones) have been measured in the sediments of the New York Bight. Range: 50 ppm organic silicon, dry weight basis, to below detection limit. Silicones are 37.9% silicon. Silicones correlated well ($r > 0.90$) with other organic constituents in the same sediment samples which have been used to characterize sewage inputs to the sediments. Silicones are offered as a totally synthetic, specific, chemical tracer for anthropogenic additions to the environment.

MATERIAL SCIENCE AND TECHNOLOGY

19. **"Anomalous Infrared Absorptance of Aluminum Under Pulsed 10.6-μm Laser Irradiation in Vacuum,"** by J. A. McKay and J. T. Schriempf, *Appl. Phys. Lett.* **35**(6):433-434, Sept. 15, 1979.

Above a distinct threshold laser flux of 70-MW/cm^2 peak (for a pulse consisting of a 150-ns spike and a 1.8-μs tail), the calorimetrically measured effective absorptance of unpolished 3003 alloy aluminum increases abruptly to roughly 14%. While too high to be ascribed to ordinary metal infrared absorptance at any reasonable temperature, this value is typical of total-energy thermal coupling in air with air plasma ignition. We propose that this absorptance is in face due to the ignition of a plasma in metal vapor produced by thermally isolated metal defects, rather than to a metal-dielectric transition.

OCEAN TECHNOLOGY

20. **"Transient Response of Two Fluid-Coupled Cylindrical Elastic Shells to an Incident Pressure Pulse,"** by H. Huang, *J. Appl. Mech.* **46**(3):513-518, Sept. 1979.

The transient response of a system of two initially concentric circular cylindrical elastic shells coupled by an ideal fluid and impinged upon by an incident plane pressure pulse is studied. The classical techniques of separation of variable and Laplace transforms are employed for simultaneously solving the wave equations governing the fluid motions and the shell equations of motion. The transformed solutions are arranged in such a manner that their inverse transforms can be accurately calculated by solving a set of Volterra integral equations in the time domain. A sample calculation of

shell responses was performed and results are compared to the case in which the outer shell is absent. It is found that the primary effects of a thin outer shell could be estimated by simple asymptotic formulas.

OPTICAL SCIENCES

21. **"Acoustic Sensitivity of Single-Mode Optical Power Dividers,"** by S. K. Sheem and J. H. Cole, *Opt. Lett.* **4**(10):322-324, Oct. 1979.

The acoustic sensitivity of previously reported evanescent-field fiber couplers has been measured. The measured values were substantially larger than the values calculated from our theoretical model. A qualitative explanation of this discrepancy is presented.

22. **"Temperature-Dependent Absorption Processes in the XeF Laser,"** by L. F. Champagne, *Appl. Phys. Lett.* **35**(7):516-519, Oct. 1, 1979.

Temperature-dependent absorption processes in neon/xenon/NF_3 mixtures are reported. In pure neon plasmas there are two types of absorption present; a broad but weak band of absorption is observed, which increases with increasing temperature, and a strong narrow band of absorption is observed around 351 nm. Moderate heating reduces this absorption. Improved performance of the XeF laser at elevated temperature is primarily due to reduced absorption in the laser medium at 351 nm.

PLASMA PHYSICS

23. **"The Electron Cyclotron Maser as a High-Power Traveling Wave Amplifier of Millimeter Waves,"** by J. L. Seftor, V. L. Granatstein, K. R. Chu, P. Sprangle, and M. E. Read, *IEEE J. Quantum Electron.* **QU-15** (9):848-853, Sept. 1979.

The electron cyclotron maser instability has been exploited as the basis for a new type of traveling wave amplifier which operates at unusually high power levels at millimeter wavelengths. The first experimental model of this amplifier has been operated at 35 GHz and has demonstrated a stable gain of 17 dB and an output power of 10 kW (unsaturated). The gain was linear over a dynamic range $>$ 30 dB. The absolute value of the gain and its dependence on current and magnetic field were in excellent agreement with theoretical calculations. Bandwidth and saturated power have yet to be measured directly, but no fundamental problems were observed which will prevent successful achievement of the design predictions (viz., bandwidth $\approx$ 10% power on the order of 10^5 W, efficiency $>$ 10%).

24. **"A Review of Recent Results on Spread F Theory,"** by S. L. Ossakow, in *Wave Instabilities in Space Plasmas*, P. J. Palmadesso and K. Papadopoulos, editors, D. Reidel, Dordrecht, 1979, pp. 265-289.

Ionospheric Spread F was discovered some four decades ago. Yet only in the past few years has significant progress been made in the theoretical explanation of such phenomena. In particular, considerable effort has been expended to explain equatorial Spread F and the attendant satellite signal propagation scintillation phenomena. The present review dwells mainly in this low-latitude area. The various linear plasma instabilities thought to initiate equatorial Spread F are discussed. Recent theoretical and numerical simulation studies of the nonlinear evolution of the collisional Rayleigh-Taylor instability in equatorial Spread F are reviewed. Also, analytical studies of rising equatorial Spread F bubbles in the collisional and collisionless Rayleigh-Taylor regime are discussed, as well as the nonlinear saturation of instabilities in these two regimes. Current theories on very small scale ($\lesssim$ 10 meters) size irregularities observed by radar backscatter during equatorial Spread F and their relation

to the larger wavelength scintillation-causing irregularities are discussed. Applications of turbulence theory to equatorial Spread F phenomena are reviewed. Remaining problems to be dealt with at equatorial latitudes are summarized.

25. **"Status of the Upgraded Version of the NRL Gamble II Pulse Power Generator,"** by J. R. Boller, J. K. Burton, and J. D. Shipman, Jr., in *Digest of Papers 2nd IEEE International Pulsed Power Conference*, Lubbock, Tex., June 1979, pp. 205-208.

The GAMBLE II water-dielectric pulse-power generator, in 1970, was the forerunner of the high-energy (> 50 kJ) class of water-dielectric generators. It has been redesigned internally to make maximum use of its original outer conductor shell and to optimize it for the positive polarity mode of operation for positive ion beam experimentation. The new design also initiates the use of an oil-dielectric multichannel switch at the output of the pulse-forming line. This switch, because of its low capacitance, eliminates the need for an extra prepulse switch. The upgraded version has been tested up to power and energy levels which are nearly twice the original.

RADAR

26. **"Reflective Butler Matrices,"** by J. P. Shelton and J. K. Hsiao, *IEEE Trans. Antennas Propag.* **AP-27** (5):651-659, Sept. 1979.

A conventional Butler matrix can be modified to achieve a network which is symmetric about an axis midway between the input and output lines. Such a Butler matrix network can be further modified so that the input and output ports are identical. In this manner the half-matrix appropriately terminated in the plane of symmetry corresponds to a reflection-type system in which the feed positions are in the aperture region. This paper describes the modifications which make the Butler matrix symmetric and the method for terminating the network on the symmetry plane so as to achieve a reflective matrix. A computer program has been written to generate and plot these network configurations.

RADIATION TECHNOLOGY

27. **"Statistical Treatment of Damage Factors for Semiconductor Devices,"** by A. I. Namenson, *IEEE Trans. Nucl. Sci.* **NS-26**(5):4691-4694, Oct. 1979.

By fitting a lognormal distribution to the data of Messenger and Steele a statistical analysis derives a formula for the survival probability, with 90% confidence, of a silicon transistor exposed to the neutron flux ϕ as

$$P_s(\phi) = F_n\left[\frac{\ln(\text{C.T.F.} - 1) + \ln\left(\frac{f_{T\min}/\beta_{\min}}{\phi}\right) + 16.38}{0.493}\right],$$

where F_n is the standard normal cumulative distribution function, C.T.F. is the circuit tolerance factor, $f_{T\min}$ is the minimum-gain bandwidth product specified by the manufacturer, and $\beta_{\min}$ is the minimum current gain specified by the manufacturer. The present analysis is similar to the previous one, except that the analysis here accounts for the fact that a lognormal distribution does not exactly fit the data. The formula shown above differs from a previous one in that the denominator of 0.444 has been replaced by 0.493. The new denominator can increase previously estimated failure probabilities by a factor of 2.5. The method shown here is generally applicable to cases where distributions other than the lognormal ones are fitted to a set data.

28. **"Submicrosecond X-Ray Lithography,"** by D. J. Nagel, M. C. Peckerar, R. R. Whitlock, J. R. Grieg, and R. E. Pechacek, *Electron. Lett.* **14**(24):781-782, Nov. 23, 1978.

X rays from laser-heated plasmas were used to replicate features as fine as 750 nm in the positive resist polybutene-1-sulfone (p.b.s.). The measured sensitivities of p.b.s. to pulsed and d.c. X-rays ($\approx 10^9$ ratio in exposure rate) are similar (no reciprocity loss). Laser-plasma x rays produced only small (0.25 V) flat-band shifts in m.o.s. capacitors at irradiation levels sufficient to expose p.b.s.

SPACE SCIENCE

29. **"Design of a Small Thermochemical Receiver for Solar Thermal Power,"** by T. A. Chubb, J. J. Nemecek and D. E. Simmons, *Sol. Energy* **23**:217-221 (1979).

Capture of solar thermal energy by means of chemical conversion provides an attractive means for collection of solar energy. A converter has been designed for operation at the focus of a 7-m-diameter paraboloid. The converter is constructed from a multipassage ceramic extrusion, which is wound into a spiral form prior to firing. The innermost wrap is designed to operate with a cavity-facing surface heated to 1000°C. In the passages adjacent to this surface SO_3 is catalytically dissociated into SO_2 and O_2. The eight outer wraps are used for heat exchange between an inflowing SO_3-rich gas stream and an outflowing SO_2-rich gas stream.

30. **"The Relative Intensity and Velocity of SiO $J = 1 \rightarrow 0$, $v = 1$ and 2 Masers,"** by P. R. Schwartz, J. A. Waak, and J. M. Bologna, *Astron. J.* **84**(9):1349-1356, Sept. 1979.

The SiO $J = 1 \rightarrow 0$, $v = 1$ and 2 maser transitions were observed nearly simultaneously with accurate cross calibration in a sample of sources. The integrated and peak intensity of the two masers are comparable and many precise velocity agreements are seen in individual features. Broad emission plateaus are seen in both the $v = 1$ and 2 transitions. These results strongly suggest that the two masers share a common pump source and are spatially coincident in a spherical mass loss flow. A strong, variable feature at $V_R = +5$ km s^{-1} was observed in Orion which may indicate the presence of a second distinct source.

PAPERS PRESENTED AT RECENT SCIENTIFIC MEETINGS

"Active Arrays–Performance Prediction," by T. L. Ap Rhys, Antenna Measurements Techniques Association, Atlanta, Ga., Oct. 17, 1979

"Ammonia as a Unique Probe of the Interstellar Environment," by D. N. Matsakis, E. O. Hulbert Center for Space Research Colloquium, Washington, D. C., Oct. 11, 1979

"Analysis of Phase Growth in a Viscoelastic Liquid," by R. Y. Ting, Society of Rheology Golden Jubilee Meeting, Boston, Mass., Oct. 28-Nov. 2, 1979

"Application of Hall-Effect Inductive Switching to Quasi-Steady MPD Arcjets," by P. J. Turchi, 14th International Electric Propulsion Conference, AIAA/DGLR, Princeton, N.J., Oct. 30-Nov. 1, 1979

"Cathodoluminescence Studies of Oxides on GaAs and Si," by S. W. McKnight, General Electric Research Laboratory, Schenectady, N.Y., Oct. 10, 1979

"Characteristics of CMOS/SOS LSI Devices at High Temperature (260°C) for Aircraft-Engine Control Applications," by L. J. Palkuti and W. L. Morris, IEEE SOS Workshop, Carefree, Ariz., Oct. 2-4, 1979

"Computationally Efficient Time Integration Methods," by R. V. Madala, 4th Conference on Numerical Weather Prediction, Silver Spring, Md., Oct. 29-Nov. 1, 1979

"Conformations of Peptides and Peptide Ion Carriers in the Crystalline State," by I. L. Karle, invited lecture, Cornell University, Ithaca, N.Y., Oct. 18, 1979

"**The Development of Radar at the Naval Research Laboratory**," by D. K. Allison, 4th Naval History Symposium, Annapolis, Md., Oct. 25-26, 1979

"**Effects of H_2, H_2O, and CO Pretreatment in the Catalytic Decomposition of Formic Acid on Platinum**," by D. E. Tevault and M. C. Lin, American Chemical Society Meeting, Roanoke, Va., Oct. 24-26, 1979

"**Electrostatic Hazards in Fuel Handling**," by J. T. Leonard, Conference on Electrostatic Hazards in the Storage and Handling of Powders and Liquids, Chicago, Ill., Oct. 16-17, 1979

"**Enhanced Raman Scattering from a Thin Organic Film on a Metal Substrate in Ultrahigh Vacuum**," by R. R. Smardzewski, R. J. Colton, and J. S. Murday, 5th Inertial Guidance Contamination Control Community Seminar, Los Angeles, Calif., Oct. 16-18, 1979

"**ESR Studies of a BeF_2 Glass**," by D. L. Griscom, M. Stapelbroek, and M. J. Weber, Fall Meeting, Glass Division, American Ceramic Society, Bedford, Pa., Oct. 10-12, 1979

"**High-Speed Fiber-Brush Operation**," by W. H. Lupton, 4th DARPA Advanced Current Collection Workshop, Pittsburgh, Pa., Oct. 24-26, 1979

"**Holography in Photoelasticity**," by R. J. Sanford, SESA Fall Meeting, Kings Island, Ohio, Oct. 7-10, 1979

"**Internal Reflection Spectroscopy and the Silicon Inversion Layer**," by R. T. Holm, Eastern Analytical Symposium, New York, Oct. 31-Nov. 2, 1979

"**Laser Heating in Semiconductors**," by J. R. Meyer, F. J. Bartoli, and M. R. Kruer, Conference on Laser-Induced Nucleation in Solids, Mons, Belgium, Oct. 4-6, 1979

"**Perspectives on Future Engineering Needs**," by M. I. Skolnik, Johns Hopkins University, Baltimore, Md., Oct. 19, 1979

"**Semiempirical Calculation of Excitation Functions**," by E. L. Petersen, International Conference on Nuclear Cross Sections for Technology, Knoxville, Tenn., Oct. 22-29, 1979

"**Signal Enhancement in Liquid-State NMR by *J* Cross-Polarization**," by G. C. Chingas, A. N. Garroway, W. B. Moniz, and R. D. Bertrand, 11th Southeastern Magnetic Resonance Conference, Gainesville, Fla., Oct. 4-5, 1979

"**Sound Speed Inversion in a Waveguide**," by J. A. DeSanto, Symposium on Ill-Posed Problems: Theory and Practice, University of Delaware, Newark, Del., Oct. 2-6, 1979

"**Sustained-Load Crack Growth Rate Measurements in Ti-6Al-4V**," by D. A. Meyn, Joint ASTM E9-E24 Fall Meeting, Pittsburgh, Pa., Oct. 29-31

3rd ASTM-EURATOM Symposium on Reactor Dosimetry
Ispra, Italy, Oct. 1-5, 1979

"**Notch-Ductility Degradation of Low-Alloy Steels with Low-to-Intermediate Neutron Fluence Exposures**," by J. R. Hawthorne

"**Review of IAEA Specialists' Meeting on Irradiation Embrittlement, Thermal Annealing, and Surveillance of Reactor Vessels**," by L. E. Steele

American Vacuum Society Annual Meeting
New York, N.Y., Oct. 2-5, 1979

"**A Composition Analysis of Nitrogen-Implanted 18/8 Stainless Steel**," by I. L. Singer, J. S. Murday, and C. R. Gossett

"**Effects of Deposition Parameters on the Properties of Superconducting RF Reactively Sputtered NbN Films**," by S. A. Wolf, I. L. Singer, E. Cucauskas, and T. L. Francavilla

"**Enhanced Raman Scattering from a Thin Organic Film on a Metal Substrate in Ultrahigh Vacuum**," by R. R. Smardzewski, R. J. Colton, and J. S. Murday

RADC Spectrum Estimation Workshop
Rome Air Development Center
Rome, N.Y., Oct. 3-5, 1979

"**Accuracy of Spectral Estimates of Band-Limited Signals**," by W. B. Gordon
"**Minimum Cross-Entropy Spectral Analysis–Introduction and Examples**," by J. E. Shore and R. W. Johnson
"**A Unifying Model for Spectral Estimation**," by C. L. Byrne and R. M. Fitzgerald

IEEE EASCON '79
Arlington, Va., Oct. 8-11, 1979

"**Environmental Effect on Precision Monopulse Instrumentation Tracking Radar at 35 GHz**," by D. C. Cross, D. D. Howard, M. Lipka, A. Mays, and E. Ornstein
"**Radiometric Measurements of Targets and Clutter**," by J. P. Hollinger, B. E. Troy, and B. S. Yaplee

Optical Society of America Annual Meeting
Rochester, N.Y., Oct. 8-12, 1979

"**The Effect of Diffusion-Pump-Oil Contamination on Diffraction-Grating Efficiency in the Vacuum-Ultraviolet Spectral Region**," by W. R. Hunter and D. W. Angel
"**Radiation from Fluctuating Three-Dimensional Scalar Sources**," by W. H. Carter and E. Wolf

32nd Annual Gaseous Electronics Conference
Pittsburgh, Pa., Oct. 9-12, 1979

"**Destruction of XeCl (X) Molecules by Rare-Gas and HCl Collisions**," by R. W. Waynant and J. G. Eden
"**Excitation Kinetics in Mercuric Halide Dissociation Lasers**," by R. Burnham
"**Excited-Species Absorption in the UV Wing of the Kr_2F^* Band**," by J. G. Eden, R. S. F. Chang, and L. J. Palumbo
"**406-nm Ar-N_2 Laser**," by J. G. Eden
"**Temporal Fluorescence Measurements for E-Beam-Excited XeCl**," by R. W. Waynant and L. J. Palumbo

American Ceramic Society Fall Meeting
New Orleans, La., Oct. 14-17, 1979

"**Internal Phase Changes in Dense Si_3N_4 Associated with High-Temperature Oxidation**," by W. J. McDonough, P. E. D. Morgan, and C. Cm. Wu
"**Weight Gain and Strength Degradation of Si_3N_4 with Various Additives upon Oxidation**," by C. Cm. Wu and K. R. McKinney

Electrochemical Society Meeting
Los Angeles, Calif., Oct. 14-19, 1979

"**Use of Activity Coefficients to Calculate the Equilibrium Conditions within a Localized Corrosion Cell on Iron**," by E. McCafferty
"**X-Ray Topography Studies of Polysilicon and Aluminum Gate MOS Capacitors**," by G. W. Anderson, P. R. Reid, N. S. Saks, W. D. Baker, and H. F. Schaake

Short Course on Fracture Control Technology
University of Wisconsin-Madison
Madison, Wis., Oct. 15-17, 1979

"**Metal Fatigue as Related to Fracture**," by T. W. Crooker
"**The Plane-Strain Stress-Intensity Test**," by R. J. Goode
"**The Ratio Analysis Diagram**," by R. J. Goode

Short Course on Metal Fracture and Fatigue
The George Washington University
Washington, D.C., Oct. 15-19, 1979

"**Fatigue-Crack Propagation: Mechanical and Metallurgical Concepts**," by G. R. Yoder
"**Fatigue-Crack Propagation: Principles for Engineering Analysis**," by T. W. Crooker

Topical Meeting on Integrated and Guided-Wave Optics
Incline Village, Nev., Oct. 19, 1979

"**Applications of Ion Implantation to Integrated Optical Spectrum Analyzers**," by W. K. Burns, J. Comas, and R. P. Moeller
"**High-Efficiency Single-Mode Fiber/Channel Waveguide Flip-Chip Coupling**," by S. K. Sheem, C. H. Bulmer, R. P. Moeller, and W. K. Burns
"**Instability of Single-Mode Communication Systems Due to Interference and Polarization Effects**," by S. K. Sheem and T. G. Giallorenzi
"**Linear Interferometric Modulator for Electromagnetic Field Detection**," by C. H. Bulmer, W. K. Burns, and R. P. Moeller
"**Low-Frequency Noise in Fiber-Coupled Diode Lasers**," by R. O. Miles, W. K. Burns, and T. G. Giallorenzi
"**Optical Waveguide Channel Branches in Ti-Diffused $LiNbO_3$**," by W. K. Burns, R. P. Moeller, C. H. Bulmer, and H. Yajima
"**Wavelength Multiplexing/Demultiplexing Using Dispersive Interferometers**," by S. K. Sheem

Electro-Optics/Laser '79 Conference
Anaheim, Calif., Oct. 23-25, 1979

"**Efficient Electronic Raman Conversion of Rare-Gas Halide Lasers**," by R. Burnham and N. Djeu
"**Laser Separation of Rare Earths in Solution**," by T. Donohue
"**Single- and Multiple-Photon Excimer-Laser-Induced Photochemistry**," by A. P. Baronavski, L. Pasternack, V. M. Donnelly, and J. R. McDonald

11th Annual Symposium on Optical Materials for High Power Lasers
Boulder, Colo., Oct. 30-31, 1979

"**Laser Damage in Yttrium Orthophosphate**," by R. Allen, L. Esterowitz, P. H. Klein, V. O. Nicolai, and W. K. Zwicker
"**Synchrotron Radiation Studies of Beryllium Fluorides**," by R. T. Williams, D. J. Nagel, P. H. Klein, and M. J. Weber

Mount Holyoke College (Lucy Pickett Lectures)
South Hadley, Mass., Oct. 31, 1979

"**Methods of Crystal Structure Analysis and Applications to Organic and Peptide Chemistry**," by I. L. Karle
"**X-Ray Crystallography and Molecules of Biological Significance: Frog Toxins and Mushroom Antitoxins**," by I. L. Karle

PATENTS

The following patents were issued during October 1979 on inventions made by employees of the Laboratory. The inventions may be used for governmental purposes without the payment of royalties to the inventors.

Multimode Electrooptic Waveguide Switch, Patent No. 4,172,630, issued Oct. 30, 1979, to William K. Burns and Thomas G. Giallorenzi.

This device is an electrooptic switch, in which one of four channel waveguides is selectively induced in a thin slab of electrooptic material by the application of an electric field between intersecting strips of electrodes disposed adjacent to the top surface of the slab and other intersecting strips of electrodes disposed adjacent to the bottom surface, directly below the top surface strips. The electrode strips comprise primary electrodes to which constant potentials are applied to induce optical paths partially through the slab and switching electrodes, vertically displaced and electrically isolated from the primary electrodes, to which alternating potentials are applied to complete the desired optical path through the slab.

Photochemical Separation of Metals in Solution by Precipitation Following Reduction or Oxidation, Patent No. 4,172,775, issued Oct. 30, 1979, to Terence Donohue.

Mixtures of metals are separated by forming salts of the metals which exhibit photoredox activity, with an anion selected to provide insoluble salts at one oxidation state and soluble salts at another oxidation state, forming a solution of these salts with a solvent selected to permit a difference in solubility of salts dissolved at different oxidation states and to be nonreactive with the nonsoluble salts, irradiating the solution with light at a wavelength which changes the oxidation state of the metal ion most susceptive to a change in oxidation state, and separating the insoluble salt formed thereby from the solution.

READER SERVICE

This page is designed to assist readers in obtaining copies of NRL reports and in ordering reprints of NRL papers published in professional journals. It also provides space for updating distribution lists and for comments or inquiries about the contents in this or previous issues of the Report of NRL Progress.

NRL Reports

Reports with AD accession (order) numbers may be purchased directly from the National Technical Information Service (NTIS), Department of Commerce, Springfield, Va. 22161. Reports with AD-L accession numbers are available only to registered patrons of the Defense Documentation Center, Cameron Station, Alexandria, Va. 22314.

Reprints

The numbers below refer to the titles and abstracts in the section, "Papers Appearing in Current Issues of Scientific Journals." To order reprint(s), circle the appropriate number(s), print your address in the space provided, sign name, and mail this page after folding and sealing it with an adhesive.

1	2	3	4	5	6	7	8	9	10	11	12
13	14	15	16	17	18	19	20	21	22	23	24
25	26	27	28	29	30						

Send Reprints to:

Distribution

Please check appropriate boxes. For changes or corrections, show old address *exactly* as it appeared on the mailing label. Recipients on the NTIS subscription list should send notices of address changes to: National Technical Information Service, U.S. Department of Commerce, Springfield, Va. 22161.

☐ Remove Name From List ☐ Change or Correct Address

Old Address:

Corrected or New Address:

Comments

Date: Signature:

FOLD HERE

Return Address:

_____

_____

_____

OFFICIAL BUSINESS
Penalty for Private Use $300

POSTAGE AND FEES PAID
DEPARTMENT OF THE NAVY
DoD-316

DIRECTOR
Naval Research Laboratory
(Code 2631)
Washington, D.C. 20375

FOLD HERE

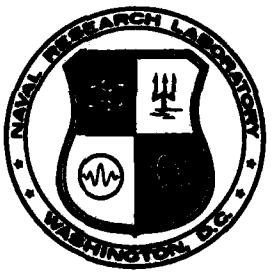

The Report of NRL Progress is published monthy at the Naval Research Laboratory. It is made available to the public through the National Technical Information Service (NTIS), Springfield, Virginia 22161. Subscription rates are $50.00 per year in the United States, Canada, and Mexico; $100.00 per year in all other countries. Single-copy rates are $6.25 in the United States, Canada, and Mexico; $12.50 all others. Issuance of this periodical approved in accordance with Department of the Navy Publications and Printing Regulations, NAVEXOS P-35. Publication will be discontinued with the December 1979 issue.

NAVSO P-3012


DA
FILM
6